MIMICAD TECHNICAL REPORT NO. 8

Electromagnetic Modeling of Coplanar Waveguide Discontinuities

by

Stephanie Petrakos

Department of Electrical and Computer Engineering
University of Colorado
Boulder, Colorado 80309-0425

Work described in this report has been supported by the MIMICAD Center and the National Science Foundation.

August 1991

Petrakos, Stephanie (M.S., Electrical and Computer Engineering)

Electromagnetic Modeling of Coplanar Waveguide Discontinuities

Thesis directed by Professor E. F. Kuester

In this thesis the Pseudo-mesh algorithm is adapted for use in CPW MMIC design. A spatial-domain mixed-potential integral equation (MPIE) and piece-wise linear roof-top basis functions serve as the foundation of this algorithm. The MPIE and Green's functions are derived for the open coplanar waveguide. The magnetic and electric Green's functions are simplified to one-dimensional Sommerfeld integrals. The MPIE is solved for the magnetic current distribution with the Galerkin method. One of the distinctive features of P-mesh is the choice of roof-top basis functions for rectangular and triangular cells as the sub-domain basis functions. This allows for a more flexible and intuitive method of gridding structures.

To characterize a network, the current distribution is sampled and the scattering parameters computed. An odd/even mode source excitation excites the network and a three-point curve-fitting technique in conjunction with a network connection algorithm is used to solve for the scattering parameters.

A program to calculate the CPW Green's functions, by Ahmad Hoorfar, was combined with a modified version of the P-mesh code. This CPW P-mesh FORTRAN program is used to analyze some passive networks. The results are found to compare well with experimental results.

ACKNOWLEDGEMENTS

I would like to thank Prof. Kuester and Prof. Chang for their guidance in this project. I would also like to thank Dr. Xian-Xiong Zheng, who developed and coded the P-mesh algorithm, and Dr. Ahmad Hoorfar, who first derived the CPW Green's functions and who wrote the program to calculate these functions.

The assistance of John Moore, David Jahn and the other students and staff of the MMICAD Center is greatly appreciated. Finally, I'd like to thank Davin and my family.

CONTENTS

FIGURES

FIGURE

CHAPTER 1

INTRODUCTION

1.1 Background

Monolithic microwave/millimeter-wave integrated circuits (MMICs) unite planar transmission line structures with active and passive components on one chip, resulting in smaller, cheaper and higher quality circuits than were previously available with the traditional microwave/millimeter-wave circuits characterized by hollow waveguides and coaxial lines. The most common planar transmission-lines used in MMIC fabrication are microstrips, coplanar waveguides (CPWs), coplanar strips (CPSs) and slotlines. These planar structures are the building blocks of MMICs which serve as detectors, mixers, couplers and amplifiers, to name a few.

In the design of MMICs, CPWs are often overlooked in favor of microstrips. Microstrips are easily adaptable to different circuit structures and a good deal is known about how they operate . In the past, lack of accurate design equations and tools for modeling CPW discontinuities and high frequency operation has limited CPW applications. Because MMICs lack the tuning capability of more traditional circuits it is necessary to develop a modeling tool for CPWs which achieves the desired performance with a minimum number of design iterations, many such CAD programs are presently available for microstrips. A full-wave simulator for open CPWs, based on the Pseudo-mesh (P-mesh) algorithm [1], is developed in this thesis.

An open coplanar waveguide consists of a conductor with two identical slots of width, w, which are separated by a distance, s. This conductor sits on one or two dielectric slabs (see Figure 1.1). For the CPW mode, the desired mode of operation, the inner conductor serves as a positive reference while the outer conductors are grounded (see Figure 1.2). The mode of propagation is quasi-TEM except at higher frequencies where the field has longitudinal components.

The physical layout of the CPW offers inherent advantages over other open waveguide structures. With all the conductors in one plane the CPW is convenient for both shunt and series insertions of active and passive components. Eliminating the need for via holes, common in microstrip structures, greatly simplifies MMIC fabrication. Parasitic inductance due to the grounding of FETS is also reduced [2]. Additionally, coplanar waveguides can be used at millimeter-wavelengths where microstrips would need impracticably thin substrates and, in at least one case, were shown to have equal or greater conductor loss and dispersion than coplanar waveguides [3]. These advantages make CPWs an attractive alternative to microstrips.

Applications of coplanar waveguides in integrated circuit design include detectors, balanced mixers [4], directional couplers [5] and CPW FET amplifiers for satellite communication systems [6]. CPW discontinuities are useful in filter design [7] and open and short end CPW terminations are used extensively for tuning stubs in transitions [8], as well as in the design of planar balanced mixers and detectors [9]. In the Ka band, amplifiers and a frequency doubler have been demonstrated with CPWs (see Figures 1.3 -1.5) [10].

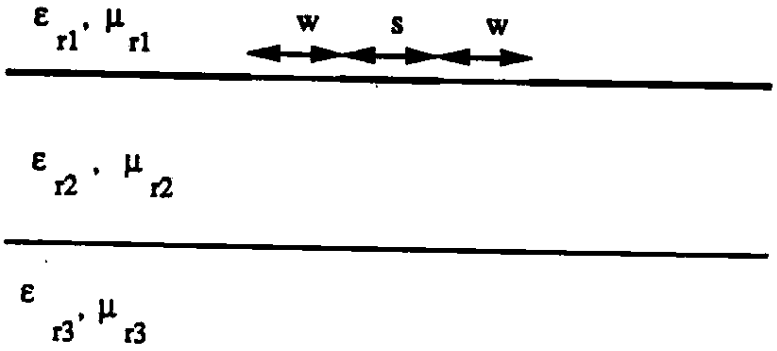

Figure 1.1: Coplanar waveguide.

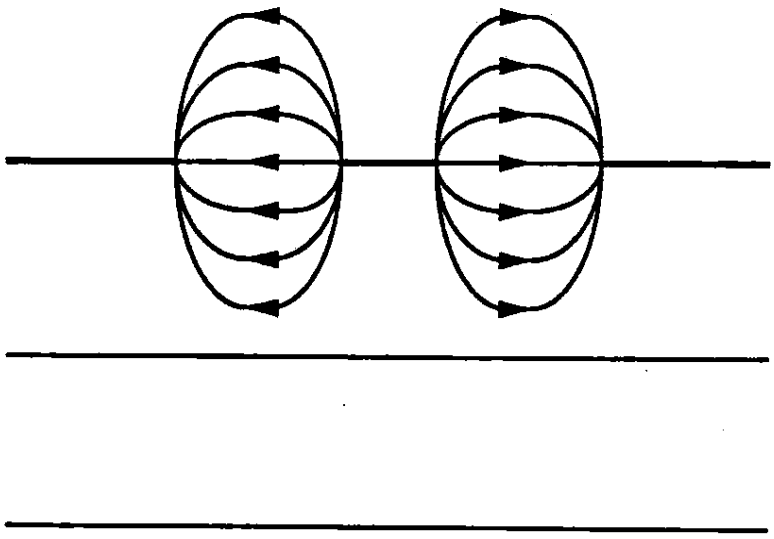

Figure 1.2: Coplanar waveguide mode

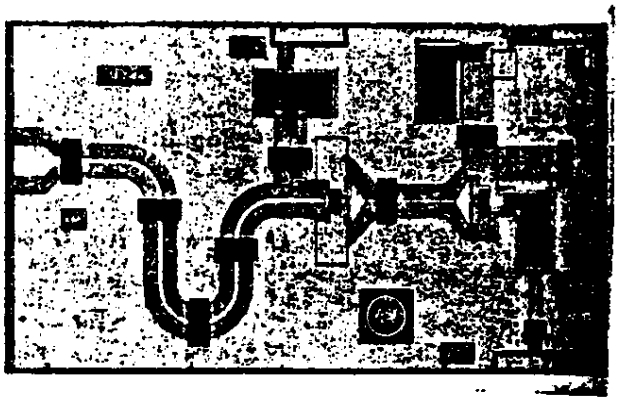

Figure 1.3: Lossy match cascode amplifier.

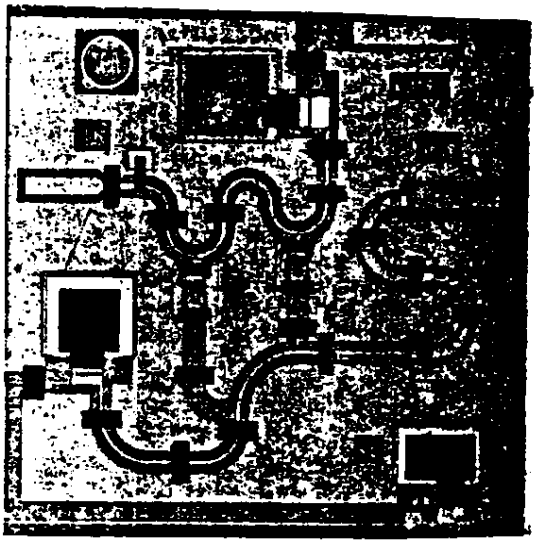

Figure 1.4: Low current distributed amplifier.

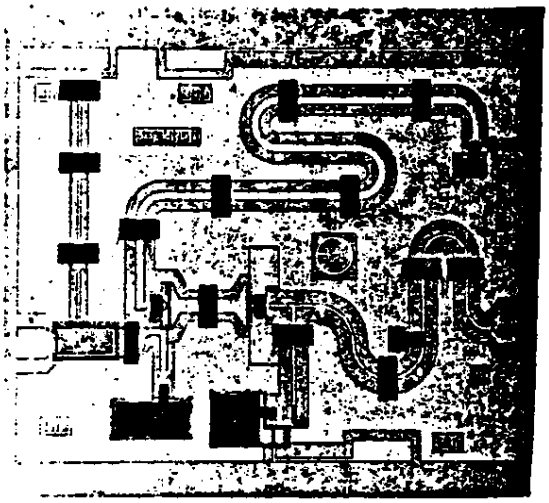

Figure 1.5: 15 to 30 GHz frequency doubler.

1.2 Methods of Analysis

Because MMICs employ open waveguides and closely placed elements, conventional transmission-line theory is no longer an adequate guide to predicting circuit behavior [1]. To fully take advantage of the uses and benefits of coplanar waveguides it is necessary to accurately model the discontinuities and parasitic coupling. When Wen introduced the CPW in 1969 [11] he used conformal mapping and quasi-static approximations to model this new structure. Davis et al. [12] took this quasi-static approach further by adapting it to CPWs of finite substrate thickness. Design equations for CPWs, based on quasi-static approximations, are summarized in [13]. Although these, and other quasi-static approaches, work fairly well at low frequencies, they mask the frequency dependence of important parameters.

Various full-wave methods have been developed for CPW analysis. Two common methods of solution to differential equations are the finite-element method and the finite-difference method. Chang, Wong and Chen [4] used a variational conformal mapping technique, solved by the finite-element method, to find the frequency dependence of the effective dielectric constant and the characteristic impedance of a CPW structure. A finite-difference time-domain technique was utilized in the analysis of CPWs by Shibata and Sano [14] and capacitance of CPW discontinuities was calculated using a three-dimensional finite-difference method by Naghed and Wolff [15].

The algorithm presented in this thesis solves for the magnetic current in the slots of the CPW by developing a spatial-domain mixed-potential integral equation (MPIE). From the moment method solution to this integral equation, which incorporates rectangular and triangular roof-top basis functions, the

scattering matrix, as well as the effective dielectric constant and the waveguide wavelength, are de-embedded.

Other methods of analysis have also centered upon integral equations solved with the moment method [16]. The integral equation techniques differ from the finite-difference and finite-element methods in that they solve a two-dimensional problem instead of a three-dimensional one. This results in fewer unknowns and a faster program. Knorr and Kuchler [17] used a integral equation moment method approach on uniform structures. Space domain integral equations, similar to the one presented in this thesis, have been developed and evaluated with the moment method in [9] and [18] to study end effects and CPW discontinuities, respectively. The major difference between these methods and the CPW P-mesh method is the choice of basis and test functions. Because the former methods are limited to only rectangular cells, they lack the versatility to model arbitrary shaped structures efficiently.

1.3 Configuration of Chapters

In Chapter 2 the background for the CPW P-mesh algorithm is discussed, an overview of the P-mesh theory and its adaptation to CPWs is presented. The MPIE for the open CPW is derived in detail in Chapter 3. In Chapter 4 the magnetic current distribution on various structures is analyzed and the method used to "extract" the scattering parameters from the full-wave solution for the magnetic current is given. Chapter 5 is composed of the P-mesh derived data for a variety of CPW structures and comparisons to measured and theoretical data from other sources.

In this algorithm it is assumed the the conductors are infinitely thin and perfectly conducting. The dielectrics in regions 1 and 3 are assumed to be

semi-infinite.

CHAPTER 2

P-MESH THEORY

2.1 Introduction

A spatial-domain mixed-potential integral equation(MPIE) and piecewise linear roof-top basis functions serve as the foundation of the P-mesh algorithm. This algorithm was developed by Zheng, Chang and Wu ([1], [19]-[21]) for application to planar transmission-line structures with an emphasis on microstrips. Using a full-wave method for numerical modeling, P-mesh provides physical insight into complex microstrip structures, taking into account both parasitic coupling and discontinuities. The scattering parameters for the structure are "de-embedded" from the full-wave solution [21].

The P-mesh algorithm for coplanar waveguides mirrors that for microstrip structures in many respects. Since adapting the original theory to coplanar waveguides is the goal of this project, the major changes necessary will be given in detail in the following chapters. However, for the sake of completeness, a summary of general P-mesh theory, common to both microstrip and CPW, will be presented here, with some minor changes to the original theory duly noted. The reader is referred to [1] for a more in-depth discussion of these topics.

2.2 Pseudo-Mesh Representation

Using both rectangular and triangular cells the slots of the coplanar waveguide can be gridded as in Figure 2.1. Instead of electric current on the

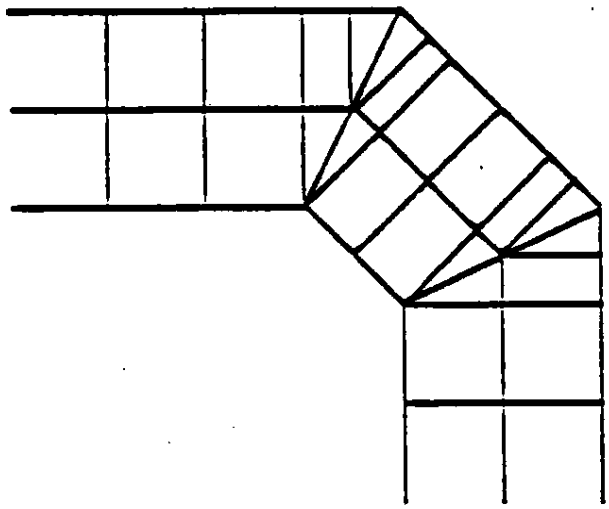

Figure 2.1. Junction modeling of a CPW slot with rectangular and triangular cells.

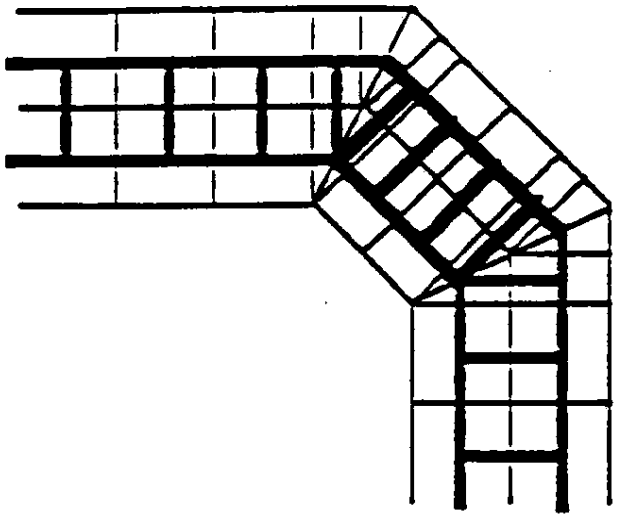

Figure 2.2: Current flow in wire mesh.

the conducting strip, as is the case for the microstrip, magnetic current in the slots is now being modeled. This magnetic current is represented by the current "mesh" shown in Figure 2.2. The normal component of the current density is assumed constant across cell boundaries. Meshes that connect to an edge are "opened" to comply with the requirement that the normal component of current (i.e., the tangential electric field) be zero at the edge. Each cell is characterized by the total current going into and coming out of each of its sides. The incoming current is not equal to the outgoing current in each cell. This current difference contributes the the charge distribution on the cell; if we insist on Kirchhoff's current law applying to nodes in the pseudo-mesh, then these charges can be thought of as residing on capacitors connected to ground.

2.3 Roof-Top Basis Functions

The scattering parameters for the coplanar waveguide are solved numerically by the moment method. The success of this method is largely dependent upon the choice of the basis functions [22]. In this case, a basis functions which most accurately approximate the magnetic current density are desired. One of the major advantages of P-mesh is the ability to combine rectangular and triangular cells in a self-consistent manner. Rectangular cells can model rectangular areas of a structure while triangular cells provide an accurate method of representing current flow around a corner, thus allowing for a more physically intuitive design for arbitrary shapes. These mixed geometries are possible as a result of the choices for the roof-top basis functions. The current distribution on rectangular and triangular cells are given in Figures 2.3 and 2.4.

2.3.1 Rectangular Roof-Top Basis Function The magnetic current density distribution in a rectangle α can be expressed [1] as

$$\bar{M}_\alpha(x,y) = \sum_{i=1}^{4} V_\alpha^{i,i+1} \bar{D}_\alpha^{i,i+1}(x,y) \tag{2.1}$$

where $V_\alpha^{i,i+1}$ is the normal component of the magnetic current density on side $(i, i+1)$ and $D_\alpha^{i,i+1}$ is the roof-top function for side $(i, i+1)$.

For the rectangular cell [1],

$$\bar{D}_\alpha^{i,i+1}(x,y) = \frac{[(y_{i+1}-y_i)(x-x_{i-1}) - (x_{i+1}-x_i)(y-y_{i-1})]}{\Delta_{i-1,i,i+1}} \cdot \frac{(x_{i-1}-x_i)\hat{x} + (y_{i-1}-y_i)\hat{y}}{d_{i-1,i}}; (x,y) \in \text{rectangle } \alpha \tag{2.2}$$

$$d_{i,j} = \sqrt{(x_i - x_j)^2 + (y_i - y_j)^2} \tag{2.3}$$

$$\Delta_{i-1,i,i+1} = \begin{vmatrix} 1 & x_{i-1} & y_{i-1} \\ 1 & x_i & y_i \\ 1 & x_{i+1} & y_{i+1} \end{vmatrix}. \tag{2.4}$$

2.3.2 Triangular Roof-Top Basis Function Similarly, the magnetic current density on a triangular cell α is represented by [1],

$$\bar{M}_\alpha(x,y) = \sum_{i=1}^{3} V_\alpha^{i,i+1} \bar{D}_\alpha^{i,i+1}(x,y) \tag{2.5}$$

where the roof-top function, $\bar{D}_\alpha^{i,i+1}$, is

$$\bar{D}_\alpha^{i,i+1}(x,y) = -\frac{d_{i,i+1}}{\Delta_{i-1,i,i+1}}[(x-x_{i-1})\hat{x} + (y-y_{i-1})\hat{y}]; (x,y) \in \text{triangle } \alpha. \tag{2.6}$$

2.3.3 Global Expression for Current Distribution The global magnetic "mesh" current, V_m, $m = 1, 2, ..., M$, where M is the number of interconnecting "meshes", can be expressed in terms of $V_\alpha^{i,i+1}$ and $V_{\alpha'}^{i',i'+1}$. For

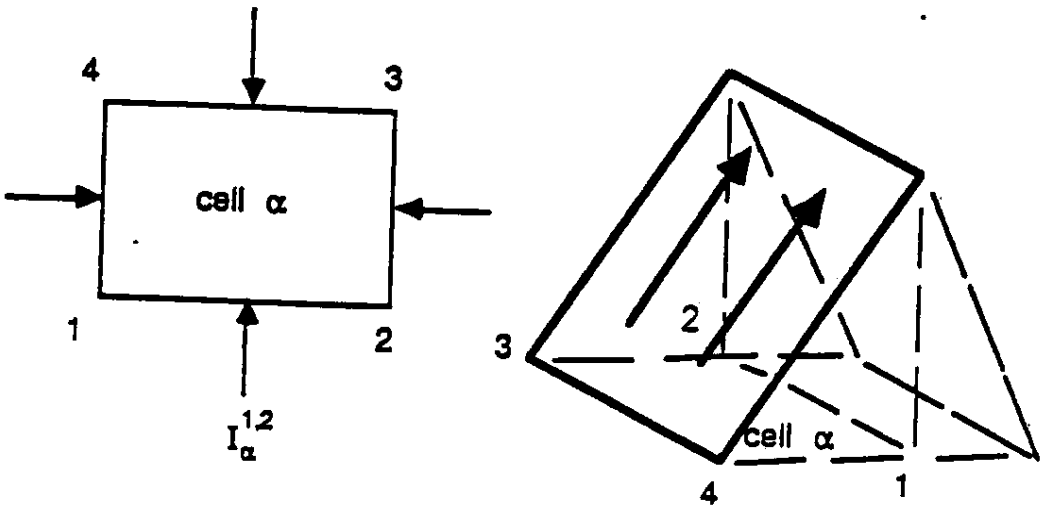

Figure 2.3: Current distribution on a rectangular cell.

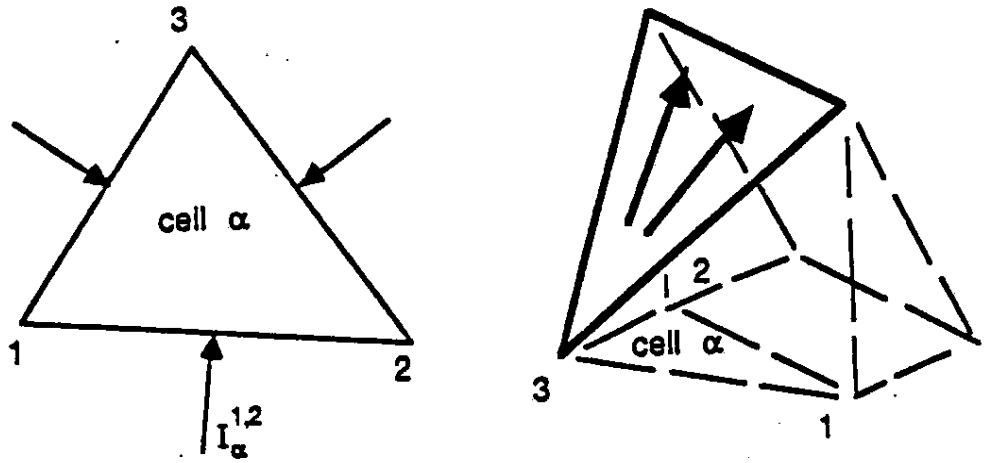

Figure 2.4: Current distribution on a triangular cell.

two adjacent cells, α and α', the common boundary can be either $(\alpha; i, i+1)$ or $(\alpha'; i', i'+1)$. The total magnetic current across the boundary is

$$V_m = V_\alpha^{i,i+1} = -V_{\alpha'}^{i',i'+1}. \tag{2.7}$$

Over the entire structure, the current distribution is [1]

$$\bar{M}(x,y) = \sum_{m=1}^{M} V_m \bar{H}_m(x,y) \tag{2.8}$$

where

$$\bar{H}_m = \bar{D}_\alpha^{i,i+1} - \bar{D}_{\alpha'}^{i',i'+1}. \tag{2.9}$$

2.4 Matrix Solution to the MPIE

The MPIE for the CPW, which will be derived in detail in Chapter 3, can be expressed as

$$\frac{k_0^2}{4\pi^2}\int_S\int_{S'}[\bar{M}_S(\bar{r})\cdot G_E(\bar{r},\bar{r}')\bar{M}_S(\bar{r}') - \frac{1}{k_0^2}\bar{M}_S(\bar{r})\cdot G_M(\bar{r},\bar{r}')\nabla_t'\nabla_t'\cdot\bar{M}_S(\bar{r}')]d\bar{r}d\bar{r}'$$
$$= -\int_S \bar{M}_S(\bar{r})\cdot\bar{H}^i(\bar{r})d\bar{r} \tag{2.10}$$

G_E and G_M are Green's functions of electric and magnetic types due to a magnetic dipole source. $\bar{r}$ is the source point and $\bar{r}'$ is the observation point. G_E and G_M are calculated numerically (Section 3.2.2).

Using Equation 2.8 in the MPIE yields the matrix equation

$$\sum_{m'=1}^{M} V_{m'} Y_{m,m'} = I_m; m = 1,2,3,...,M \tag{2.11}$$

where

$$Y_{m,m'} = \frac{k_0^2}{4\pi^2}\int_{S_m}\int_{S_{m'}}[\bar{H}_m(\bar{r}) \cdot G_E(\bar{r},\bar{r}')\bar{H}_{m'}(\bar{r}')$$
$$-\frac{1}{k_0^2}\bar{H}_m(\bar{r})\cdot G_M(\bar{r},\bar{r}')\nabla_t'\nabla_t'\cdot\bar{H}_{m'}(\bar{r}')]d\bar{r}d\bar{r}' \tag{2.12}$$

and

$$I_m = -\int_{S_m} \bar{H}_m(\bar{r}) \cdot \bar{H}^i(\bar{r}) d\bar{r}. \tag{2.13}$$

The electric current, I_m, is a function of known values and can be calculated directly. To solve for the matrix element $Y_{m,m'}$, the integrals in Equation 2.12 are put in the form,

$$\int_{cell\alpha} ds \int_{cell\alpha'} ds' G_{E,M}(\rho) x^{\mu} y^{\upsilon} x'^{\mu'} y'^{\upsilon'} \quad ;\mu,\upsilon,\mu',\upsilon' \geq 0 \text{ and } 0 \leq \mu+\upsilon, \mu'+\upsilon' \leq 1. \tag{2.14}$$

The Green's functions are calculated numerically then curve-fit into polynomials over a range of ρ (see Section 3.2),

$$G_{E,M}(\rho) = \sum_{p=-1}^{N_p} C_p^{E,M} \rho^p. \tag{2.15}$$

Using this semi-analytic expression for the Green's function, the integrals in Equation 2.14 reduce to

$$Q(\alpha,\alpha',\mu,\upsilon,\mu',\upsilon',\rho) = \int_{cell\alpha} ds \int_{cell\alpha} ds' \rho^p x^{\mu} y^{\upsilon} x'^{\mu'} y'^{\upsilon'} \quad ;p = -1, 0, ..., N_p. \tag{2.16}$$

From this quadruple integral the admittance matrix is calculated. With $Y_{m,m'}$ and I_m known, the magnetic current or voltage, $V_{m'}$, is computed.

CHAPTER 3

THE COPLANAR WAVEGUIDE MIXED POTENTIAL INTEGRAL EQUATION

3.1 Introduction

In order to solve for the scattering at a junction, the junction must first be represented adequately. For the CPW the mixed potential integral equation is chosen to characterize the fields of an arbitrary structure. First introduced by Harrington [16], the MPIE offers a variety of advantages over other methods. It is valid for all frequencies, is numerically stable and can be solved with efficient algorithms [22]. Because it can be analyzed in the spatial domain, the MPIE allows for good physical insight. Additionally, the Green's functions for the MPIE have singularities of $1/R$, where $R = |r - r'|$ is the distance between the source and observation points, and can be represented by one-dimensional Sommerfeld integrals for one-dimensionally layered substrates.

Derivation of the MPIE begins with the boundary conditions on the structure. An impressed magnetic dipole will produce the electric and magnetic Green's functions, G_E and G_M, respectively. In Section 3.2 the Whittaker potentials are implemented in the derivation of these Green's functions. The resultant functions, in the form of Sommerfeld integrals, can be solved with numerical integration. With G_E and G_M known, the MPIE in the spatial domain can be solved for the magnetic current. The derivation of the MPIE is carried out in Section 3.3, using the convolution theory and the moment

method. In the following derivations perfect magnetic walls in the slots are assumed and a time variation of $e^{j\omega t}$ is adopted. Because only planar structures will be analyzed the final expressions will be dependent on only x and y.

3.2 Coplanar Waveguide Green's Function

3.2.1 Solution to Whittaker Potentials The coplanar waveguide is shown in Figure 3.1. The scattered electric field in the slots can be represented by a magnetic current with the aperture metalized over (see Figure 3.2). Using the Whittaker potentials [23], the tangential field components for this structure are:

$$\bar{E}_t = \nabla_t \frac{\partial V}{\partial z} - j\omega\mu_n \nabla_t \times (\hat{z}U) \tag{3.1}$$

$$\bar{H}_t = \nabla_t \frac{\partial U}{\partial z} + j\omega\epsilon_n \nabla_t \times (\hat{z}V) \tag{3.2}$$

where

$$\nabla_t = \hat{x}\frac{\partial}{\partial x} + \hat{y}\frac{\partial}{\partial y} \tag{3.3}$$

and n denotes the dielectric region.

The wave equation,

$$(\nabla^2 + k_n^2)\begin{Bmatrix} \bar{U} \\ \bar{V} \end{Bmatrix} = 0 \tag{3.4}$$

with

$$k_n = \sqrt{\omega^2\mu_n\epsilon_n} \tag{3.5}$$

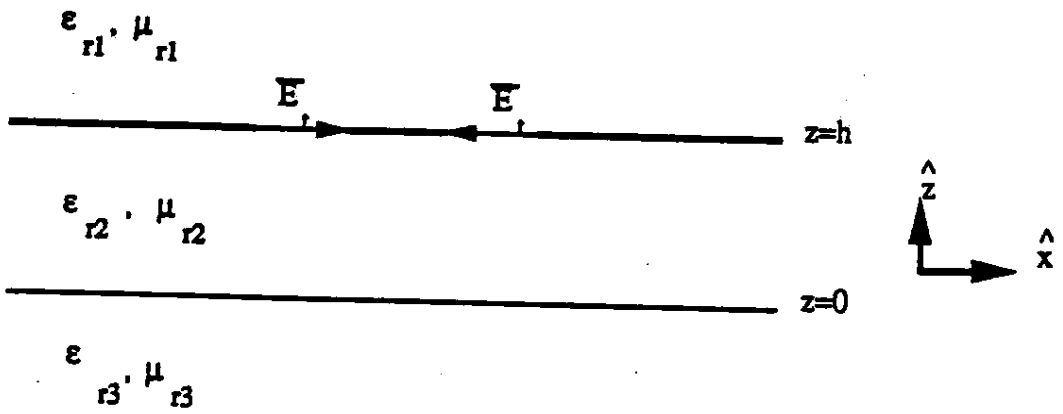

Figure 3.1: Coplanar waveguide with three dielectric regions.

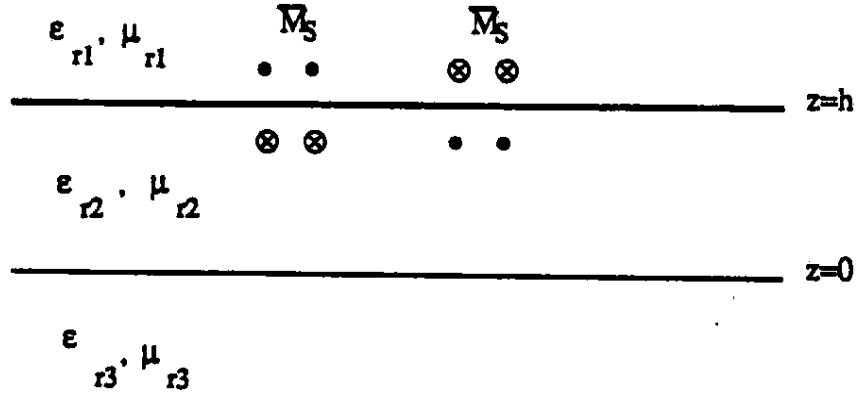

Figure 3.2: Coplanar waveguide equivalent circuit.

is true for all three regions. Taking the double-Fourier transform,

$$F(x,y) = \int\int_{-\infty}^{+\infty} \tilde{\tilde{F}}(\alpha,\beta) e^{-jk_0(\alpha x+\beta y)} d\alpha d\beta, \tag{3.6}$$

the wave equation becomes

$$(\frac{\partial^2}{\partial z^2} - k_0^2 u_n^2) \left\{ \begin{array}{c} \tilde{\tilde{U}} \\ \tilde{\tilde{V}} \end{array} \right\} = 0 \tag{3.7}$$

where

$$u_n = \sqrt{(\alpha^2+\beta^2) - \epsilon_{rn}\mu_{rn}} \tag{3.8}$$

and

$$\Re(u_n) > 0 \qquad \text{for} \qquad \alpha^2+\beta^2 > \epsilon_{rn}\mu_{rn}^2. \tag{3.9}$$

The solutions to the ordinary differential equations above, for $\tilde{\tilde{U}}$ and $\tilde{\tilde{V}}$, are [23]:

$$\tilde{\tilde{U}} = \left\{ \begin{array}{ll} A_U e^{k_0 u_1 z} & z > h \\ B_U e^{-k_0 u_2 z} + C_U e^{k_0 u_2 z} & 0 < z < h \\ D_U e^{-k_0 u_3 z} & z < 0 \end{array} \right. \tag{3.10}$$

$$\tilde{\tilde{V}} = \left\{ \begin{array}{ll} A_V e^{k_0 u_1 z} & z > h \\ B_V e^{-k_0 u_2 z} + C_V e^{k_0 u_2 z} & 0 < z < h \\ D_V e^{-k_0 u_3 z} & z < 0 \end{array} \right. \tag{3.11}$$

$A_{U,V}$, $B_{U,V}$, $C_{U,V}$and $D_{U,V}$ are unknowns.

To derive $\tilde{\tilde{U}}$ and $\tilde{\tilde{V}}$, the boundary conditions for the structure are needed. At $z = 0$,

$$\tilde{E}_t \text{ is continuous} \tag{3.12}$$

$$\tilde{H}_t \text{ is continuous.} \tag{3.13}$$

In the spectral domain the tangential electric field is represented by,

$$\tilde{\bar{\bar{E}}}_t = \tilde{\nabla}\frac{\partial \tilde{\bar{\bar{V}}}}{\partial z} - j\omega\mu_n \tilde{\nabla}_\perp(\tilde{\bar{\bar{U}}}) \tag{3.14}$$

and the tangential magnetic field is given by,

$$\tilde{\bar{\bar{H}}}_t = \tilde{\nabla}\frac{\partial \tilde{\bar{\bar{U}}}}{\partial z} + j\omega\epsilon_n \tilde{\nabla}_\perp(\tilde{\bar{\bar{V}}}) \tag{3.15}$$

where

$$\tilde{\nabla} = -jk_0(\alpha\hat{x} + \beta\hat{y}) \qquad \tilde{\nabla}_\perp = -jk_0(-\alpha\hat{y} + \beta\hat{x}). \tag{3.16}$$

From the boundary conditions, $\frac{\partial \tilde{\bar{\bar{U}}}}{\partial z}$, $\frac{\partial \tilde{\bar{\bar{V}}}}{\partial z}$, $\tilde{\bar{\bar{U}}}$ and $\tilde{\bar{\bar{V}}}$ will all be continuous at $z = 0$, yielding:

$$\mu_2(B_U + C_U) = \mu_3 D_U \tag{3.17}$$

$$\epsilon_2(B_V + C_V) = \epsilon_3 D_V \tag{3.18}$$

$$u_2(B_U - C_U) = u_3 D_U \tag{3.19}$$

$$u_2(B_V - C_V) = u_3 D_V. \tag{3.20}$$

Combining these equations produces:

$$C_U = \frac{u_2\mu_{r3} - u_3\mu_{r2}}{u_2\mu_{r3} + u_3\mu_{r2}} B_U = R(\alpha,\beta)B_U \tag{3.21}$$

$$C_V = \frac{u_2\epsilon_{r3} - u_3\epsilon_{r2}}{u_2\epsilon_{r3} + u_3\epsilon_{r2}} B_V = T(\alpha,\beta)B_V. \tag{3.22}$$

At $z = h$,

$$\bar{E}_t \text{ is continuous in the slots} \tag{3.23}$$

$$\bar{M}_S = \hat{n} \times \bar{E}_t. \tag{3.24}$$

Since $\bar{E}_t$ is zero on the conductor, $\bar{\bar{\tilde{E}}}_t$ is continuous and $\bar{\bar{\tilde{M}}}_S = \hat{z} \times \bar{\bar{\tilde{E}}}_t$.

At $z = h^-$,

$$\bar{\bar{\tilde{M}}}_S(\alpha,\beta) = -k_0 u_2 \tilde{\nabla}_\perp B_V [e^{-k_0 u_2 h} - T(\alpha,\beta) e^{k_0 u_2 h}] + j\omega\mu_2 \tilde{\nabla} B_U [e^{-k_0 u_2 h} + R(\alpha,\beta) e^{k_0 u_2 h}]. \quad (3.25)$$

Dotting both sides of Equation 3.25 with $\tilde{\nabla}$ leads to the solution for B_U,

$$B_U = \frac{j\tilde{\nabla} \cdot \bar{\bar{\tilde{M}}}_S(\alpha,\beta)}{k_0^2 \omega \mu_2 (\alpha^2+\beta^2)} \left[\frac{1}{e^{-k_0 u_2 h} + R(\alpha,\beta) e^{k_0 u_2 h}} \right]. \quad (3.26)$$

In a similar manner, dotting both sides with $\tilde{\nabla}_\perp$ produces

$$B_V = \frac{\tilde{\nabla}_\perp \cdot \bar{\bar{\tilde{M}}}_S(\alpha,\beta)}{k_0^3 u_2 (\alpha^2+\beta^2)} \left[\frac{1}{e^{-k_0 u_2 h} - T(\alpha,\beta) e^{k_0 u_2 h}} \right]. \quad (3.27)$$

The remaining unknowns, A_U and A_V, are solved by forcing the tangential electric field to be continuous at $z = h$,

$$\tilde{\nabla}[-k_0 u_2 B_V (e^{-k_0 u_2 h} - T(\alpha,\beta) e^{k_0 u_2 h})] - j\omega\mu_2 \tilde{\nabla}_\perp [B_U (e^{-k_0 u_2 h} + R(\alpha,\beta) e^{k_0 u_2 h})] = \tilde{\nabla}[k_0 u_1 A_V e^{k_0 u_1 h}] - j\omega\mu_1 \tilde{\nabla}_\perp [A_U e^{k_0 u_1 h}] \quad (3.28)$$

Grouping similar terms and substituting in Equations 3.26 and 3.27, A_U and A_V can be written as

$$A_U = \frac{j\tilde{\nabla} \cdot \bar{\bar{\tilde{M}}}_S(\alpha,\beta)}{k_0^2 \omega \mu_1 (\alpha^2+\beta^2)} e^{-k_0 u_1 h} \quad (3.29)$$

$$A_V = -\frac{\tilde{\nabla}_\perp \cdot \bar{\bar{\tilde{M}}}_S(\alpha,\beta)}{k_0^3 u_1 (\alpha^2+\beta^2)} e^{-k_0 u_1 h}. \quad (3.30)$$

Substituting the values of $A_U, A_V, B_U, B_V, C_U, C_V, D_U$ and D_V into Equations 3.10 and 3.11, $\bar{\bar{\tilde{U}}}$ and $\bar{\bar{\tilde{V}}}$ for all three dielectric regions are known.

$$\bar{\bar{\tilde{U}}} = \begin{cases} \frac{j\tilde{\nabla} \cdot \bar{\bar{\tilde{M}}}_S(\alpha,\beta)}{k_0^2 \omega \mu_1 (\alpha^2+\beta^2)} e^{k_0 u_1 (z-h)} & z > h \\ \frac{j\tilde{\nabla} \cdot \bar{\bar{\tilde{M}}}_S(\alpha,\beta)}{k_0^2 \omega \mu_2 (\alpha^2+\beta^2)} \left[\frac{e^{-k_0 u_2 (z-h)} + R(\alpha,\beta) e^{k_0 u_2 (z+h)}}{1 + R(\alpha,\beta) e^{2k_0 u_2 h}} \right] & 0 < z < h \\ \frac{j\tilde{\nabla} \cdot \bar{\bar{\tilde{M}}}_S(\alpha,\beta)}{k_0^2 \omega \mu_3 (\alpha^2+\beta^2)} \left[\frac{1 + R(\alpha,\beta)}{1 + R(\alpha,\beta) e^{2k_0 u_2 h}} \right] e^{-k_0 (u_3 z - u_2 h)} & z < 0 \end{cases} \quad (3.31)$$

$$\tilde{\tilde{V}} = \begin{cases} -\frac{\tilde{\nabla}_\perp \cdot \tilde{\tilde{M}}_S(\alpha,\beta)}{k_0^3 u_1(\alpha^2+\beta^2)} e^{k_0 u_1(z-h)} & z > h \\ \frac{\tilde{\nabla}_\perp \cdot \tilde{\tilde{M}}_S(\alpha,\beta)}{k_0^3 u_2(\alpha^2+\beta^2)} \left[\frac{e^{-k_0 u_2(z-h)} + T(\alpha,\beta) e^{k_0 u_2(z+h)}}{1 - T(\alpha,\beta) e^{2k_0 u_2 h}}\right] & 0 < z < h \\ \frac{\epsilon_{r2}}{\epsilon_{r3}} \frac{\tilde{\nabla}_\perp \cdot \tilde{\tilde{M}}_S(\alpha,\beta)}{k_0 u_2(\alpha^2+\beta^2)} \left[\frac{1 + T(\alpha,\beta)}{1 - T(\alpha,\beta) e^{2k_0 u_2 h}} e^{-k_0(u_3 z - u_2 h)}\right] & z < 0 \end{cases} \tag{3.32}$$

3.2.2 Scalar Electric and Magnetic Potentials for the CPW

The last boundary condition on the CPW is the continuity of the tangential magnetic field in the slots at $z = h$. For this condition to be true

$$\bar{H}_t^s|_{h^-}^{h^+}(\bar{r}) = -\bar{H}_t^i(\bar{r}). \tag{3.33}$$

where $\bar{H}_t^s|_{h^-}^{h^+}(\bar{r})$ is the jump in the scattered tangential magnetic field and $\bar{H}_t^i(\bar{r})$ is the impressed tangential magnetic field.

In the spectral domain the tangential magnetic field is represented by,

$$\tilde{\tilde{H}}_t(\alpha,\beta) = \tilde{\nabla} \frac{\partial \tilde{\tilde{U}}}{\partial z} + j\omega\epsilon_n \tilde{\nabla}_\perp \tilde{\tilde{V}}. \tag{3.34}$$

With the values of $\tilde{\tilde{U}}$ and $\tilde{\tilde{V}}$ known, $\bar{H}_t^s|_{h^-}^{h^+}$ can be calculated in the spectral domain.

$$\begin{aligned} & j\tilde{\nabla}\left[k_0 u_1 \left(\frac{\tilde{\nabla}\cdot\tilde{\tilde{M}}_S(\alpha,\beta)}{k_0^2\omega\mu_1(\alpha^2+\beta^2)}\right)\right] + \omega\epsilon_1\tilde{\nabla}_\perp\left(\frac{-j\tilde{\nabla}_\perp\cdot\tilde{\tilde{M}}_S(\alpha,\beta)}{k_0^3 u_1(\alpha^2+\beta^2)}\right) \\ - \; & j\tilde{\nabla}\left[-k_0 u_2\left(\frac{\tilde{\nabla}\cdot\tilde{\tilde{M}}_S(\alpha,\beta)}{k_0^2\omega\mu_2(\alpha^2+\beta^2)}\right)\left(\frac{e^{-k_0u_2h} - R(\alpha,\beta)e^{k_0u_2h}}{e^{-k_0u_2h} + R(\alpha,\beta)e^{k_0u_2h}}\right)\right] \\ - \; & j\omega\epsilon_2\tilde{\nabla}_\perp\left[\left(\frac{\tilde{\nabla}_\perp\cdot\tilde{\tilde{M}}_S(\alpha,\beta)}{k_0^3 u_2(\alpha^2+\beta^2)}\right)\left(\frac{e^{-k_0u_2h} + T(\alpha,\beta)e^{k_0u_2h}}{e^{-k_0u_2h} - T(\alpha,\beta)e^{k_0u_2h}}\right)\right] \\ = \; & \tilde{\tilde{H}}_t^s|_{h^-}^{h^+}. \end{aligned} \tag{3.35}$$

Grouping similar terms and taking the inverse Fourier transform, to convert back to the spatial domain, yields

$$\iint_{-\infty}^{\infty}\left[\tilde{\bar{F}}_1(\alpha,\beta)\frac{\tilde{\nabla}\tilde{\nabla}\cdot\tilde{\bar{M}}_S(\alpha,\beta)}{k_0^2(\alpha^2+\beta^2)}+\tilde{\bar{F}}_2(\alpha,\beta)\frac{\tilde{\nabla}_\perp\tilde{\nabla}_\perp\cdot\tilde{\bar{M}}_S(\alpha,\beta)}{k_0^2(\alpha^2+\beta^2)}\right]$$
$$\times e^{-jk_0(\alpha x+\beta y)}\,d\alpha\,d\beta=\bar{H}_t^s(\bar{r})|_{h^-}^{h^+} \qquad (3.36)$$

where

$$\tilde{\bar{F}}_1(\alpha,\beta)=\frac{j}{\eta_0}\left[\frac{u_1}{\mu_{r1}}+\frac{u_2}{\mu_{r2}}\frac{u_3\mu_{r2}+u_2\mu_{r3}tanh(k_0u_2h)}{D_{\mathrm{TE}}}\right] \qquad (3.37)$$

$$\tilde{\bar{F}}_2(\alpha,\beta)=-\frac{j}{\eta_0}\left[\frac{\epsilon_{r1}}{u_1}+\frac{\epsilon_{r2}}{u_2}\frac{u_2\epsilon_{r3}+u_3\epsilon_{r2}tanh(k_0u_2h)}{D_{\mathrm{TM}}}\right] \qquad (3.38)$$

$$D_{\mathrm{TE}}=u_2\mu_{r3}+u_3\mu_{r2}tanh(k_0u_2h) \qquad (3.39)$$

and

$$D_{\mathrm{TM}}=u_3\epsilon_{r2}+u_2\epsilon_{r3}tanh(k_0u_2h). \qquad (3.40)$$

Since $\frac{\tilde{\nabla}}{jk_0(\alpha^2+\beta^2)^{\frac{1}{2}}}$ and $\frac{\tilde{\nabla}_\perp}{jk_0(\alpha^2+\beta^2)^{\frac{1}{2}}}$ are unit vectors, the following identity is true [24]:

$$\tilde{A}_t=-\frac{\tilde{\nabla}\cdot\tilde{A}_t}{k_0^2(\alpha^2+\beta^2)}\tilde{\nabla}-\frac{\tilde{\nabla}_\perp\cdot\tilde{A}_t}{k_0^2(\alpha^2+\beta^2)}\tilde{\nabla}_\perp \qquad (3.41)$$

$$\frac{\tilde{\nabla}_\perp\tilde{\nabla}_\perp\cdot\tilde{A}_t}{k_0^2(\alpha^2+\beta^2)}=-\tilde{A}_t+\frac{\tilde{\nabla}\tilde{\nabla}\cdot\tilde{A}_t}{k_0^2(\alpha^2+\beta^2)}. \qquad (3.42)$$

Using this identity in combination with Equations 3.36 and 3.33 yields,

$$\int\int_{-\infty}^{\infty}[\tilde{\tilde{G}}_E(\alpha,\beta)\tilde{\tilde{M}}_S(\alpha,\beta)-\frac{1}{k_0^2}\tilde{\tilde{G}}_M(\alpha,\beta)\tilde{\nabla}\tilde{\nabla}\cdot\tilde{\tilde{M}}_S(\alpha,\beta)]$$
$$\times e^{-jk_0(\alpha x+\beta y)}d\alpha d\beta=-\bar{H}^i(\bar{r}) \qquad (3.43)$$

where

$$\tilde{\tilde{G}}_E(\alpha,\beta)=\frac{j}{\eta_0}\left[\frac{\epsilon_{r1}}{u_1}+\frac{\epsilon_{r2}}{u_2}\frac{u_3\mu_{r2}+u_2\mu_{r3}tanh(k_0u_2h)}{D_{\mathrm{TE}}}\right] \qquad (3.44)$$

and

$$\tilde{\tilde{G}}_M(\alpha,\beta)=\frac{1}{(\alpha^2+\beta^2)}\left\{\frac{j}{\eta_0}\left[\frac{u_1}{\mu_{r1}}+\frac{u_2}{\mu_{r2}}\frac{u_2\epsilon_{r2}+u_3\epsilon_{r3}tanh(k_0u_2h)}{D_{\mathrm{TM}}}\right]\right.$$
$$\left.+\tilde{\tilde{G}}_E(\alpha,\beta)\right\}. \qquad (3.45)$$

$\tilde{\tilde{G}}_E(\alpha,\beta)$ and $\tilde{\tilde{G}}_M(\alpha,\beta)$ represent the scalar electric and magnetic potentials in the spectral domain. Taking the double Fourier transform converts the Green's functions to the spatial domain,

$$G_E(\bar{r},\bar{r'})=\int\int_{-\infty}^{\infty}\tilde{\tilde{G}}_E(\alpha,\beta)e^{-jk_0(\alpha x+\beta y)}d\alpha d\beta \qquad (3.46)$$

$$G_M(\bar{r},\bar{r'})=\int\int_{-\infty}^{\infty}\tilde{\tilde{G}}_M(\alpha,\beta)e^{-jk_0(\alpha x+\beta y)}d\alpha d\beta. \qquad (3.47)$$

Making a polar change of coordinates reduces Equations 3.46 and 3.47 to one-dimensional Sommerfeld integrals [23]. Letting

$$\alpha=\lambda\cos\chi \qquad (3.48)$$

and

$$\beta=\lambda\sin\chi \qquad (3.49)$$

results in

$$G_E(\bar{r},\bar{r}') = 2\pi \int_0^\infty \tilde{\tilde{G}}_E(\lambda^2)\lambda J_0(\lambda\rho k_0)d\lambda \tag{3.50}$$

$$G_M(\bar{r},\bar{r}') = 2\pi \int_0^\infty \tilde{\tilde{G}}_M(\lambda^2)\lambda J_0(\lambda\rho k_0)d\lambda \tag{3.51}$$

where

$$\lambda = \sqrt{\alpha^2+\beta^2} \tag{3.52}$$

and

$$\rho = \sqrt{(x-x')^2+(y-y')^2}. \tag{3.53}$$

At $\rho = 0$ both G_E and G_M have a singularity. To compute the Sommerfeld integrals accurately and efficiently the static singular term for each Green's function must first be subtracted out.

$$G_{E,M} = G^{sm}_{E,M} + G^{s}_{E,M} \tag{3.54}$$

where

$$G^s_E = \frac{-j2\pi}{\eta_0}(\epsilon_{r1}+\epsilon_{r2})\frac{1}{k_0\rho} \tag{3.55}$$

$$G^{sm}_E = 2\pi\int_0^\infty \frac{-j}{\eta_0}\lambda J_0(\lambda\rho k_0)\left[\frac{\epsilon_{r2}}{u_2}\frac{u_3\mu_{r2}+u_2\mu_{r3}tanh(k_0u_2h)}{D_{\rm TE}} + \frac{\epsilon_{r1}}{u_2} - (\epsilon_{r1}+\epsilon_{r2})\right]d\lambda \tag{3.56}$$

$$G^s_M = \frac{-j2\pi}{\eta_0}\left(\frac{1}{\mu_{r1}}+\frac{1}{\mu_{r2}}\right)\frac{1}{k_0\rho} \tag{3.57}$$

and

$$G^{sm}_M = 2\pi\int_0^\infty \frac{-j}{\lambda\eta_0}J_0(\lambda\rho k_0)\left[\frac{u_1}{\mu_{r1}}+\frac{u_2}{\mu_{r2}}\frac{u_2\epsilon_{r2}+u_3\epsilon_{r3}tanh(k_0u_2h)}{D_{\rm TM}}+\frac{\epsilon_{r1}}{u_1} + \frac{\epsilon_{r2}}{u_2}\frac{u_3\mu_{r2}+u_2\mu_{r3}tanh(k_0u_2h)}{D_{\rm TE}} - \left(\frac{1}{\mu_{r1}}+\frac{1}{\mu_{r2}}\right)\right]d\lambda. \tag{3.58}$$

In a method developed by Hoorfar (see Figure 3.3) [25], G_E^{sm} and G_M^{sm} are integrated over the real axis from 0 to λ_s, where

$$\lambda_s = Min(n_2, n_3) - 0.25 \quad ; n_i = \sqrt{\epsilon_{ri}\mu_{ri}}. \tag{3.59}$$

From λ_s to λ_e the path of integration is triangular with

$$\lambda_e = Max(n_2, n_3) - 0.20 \tag{3.60}$$

and height, h, a function of $k_0\rho$ and $k_0 t$. An averaging technique is used for real axis integration from λ_e to some λ_{max} and closed form corrections are used for the integration from λ_{max} to infinity.

When the values of G_E^{sm} and G_M^{sm} have been calculated for a set of ρ values, they are then curve-fit into polynomials over a range of ρ:

$$G_{E,M}(\rho) = \sum_{p=-1}^{N_p} C_p^{E,M} \rho^p, \tag{3.61}$$

where $C_p^{E,M}$ are the curve-fitting coefficients and N_p is the order of the polynomial.

3.3 Mixed-Potential Integral Equation

To put the MPIE,

$$\int\int_{-\infty}^{\infty} [\tilde{\bar{\bar{G}}}_E(\alpha,\beta)\tilde{\bar{\bar{M}}}_S(\alpha,\beta) - \frac{1}{k_0^2}\tilde{G}_M(\alpha,\beta)\tilde{\nabla}\tilde{\nabla}\cdot\tilde{\bar{\bar{M}}}_S(\alpha,\beta)] \times e^{-jk_0(\alpha x+\beta y)} d\alpha d\beta = -\tilde{\bar{\bar{H}}}_t^i(\bar{r}), \tag{3.62}$$

in the desired form, apply the convolution theorem,

$$\int\int_{-\infty}^{\infty} \tilde{\bar{F}}(\alpha,\beta)\,\tilde{\bar{G}}(\alpha,\beta) e^{-jk_0(\alpha x+\beta y)} d\alpha d\beta = \frac{k_0^2}{4\pi^2}\int_S F(\bar{r})\,G(\bar{r},\bar{r}')d\bar{r}'. \tag{3.63}$$

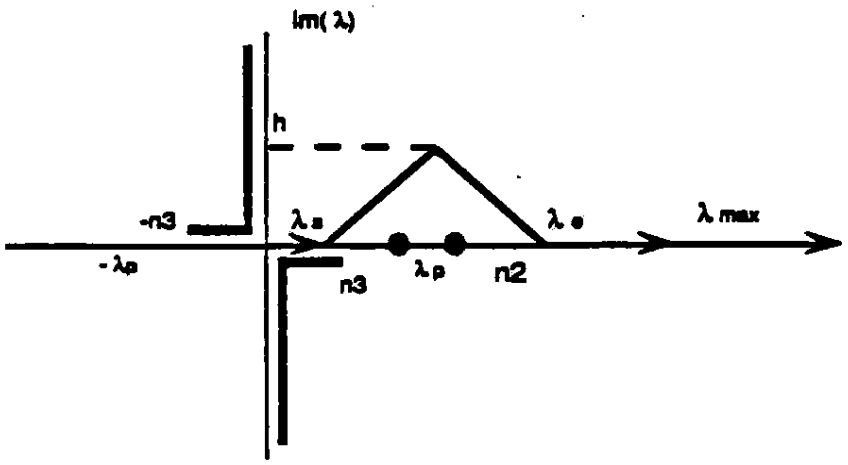

Figure 3.3: Path of integration.

The resultant equation is

$$\frac{k_0^2}{4\pi^2}\int_S \left[G_E(\bar{r},\bar{r}')\bar{M}_S(\bar{r}') - \frac{1}{k_0^2}G_M(\bar{r},\bar{r}')\nabla_t'\nabla_t'\cdot\bar{M}_S(\bar{r}')\right]d\bar{r}' = -\bar{H}_t^i(\bar{r}). \quad (3.64)$$

Using the Galerkin method, both sides of Equation 3.64 are dotted with $\bar{M}_S(\bar{r})$and integrated over the surface, S, to produce,

$$\frac{k_0^2}{4\pi^2}\int\int_S [\bar{M}_S(\bar{r})\cdot G_E(\bar{r},\bar{r}')\bar{M}_S(\bar{r}') - \frac{1}{k_0^2}\bar{M}_S(\bar{r})\cdot G_M(\bar{r},\bar{r}')\nabla_t'\nabla_t'\cdot\bar{M}_S(\bar{r}')]dr\,dr'$$
$$= -\int_S \bar{M}_S(\bar{r})\cdot\bar{H}_t^i(\bar{r})d\bar{r}. \quad (3.65)$$

G_E and G_M can be calculated, as was shown in the previous section, and $\bar{H}^i$ is known. Approximating $\bar{M}_S$ with roof-top basis functions, the MPIE can be solved for the magnetic current (see Section 2.4).

CHAPTER 4

DE-EMBEDDING OF NETWORK PARAMETERS

4.1 Introduction

Impedance, admittance and scattering parameters are all means by which a network can be characterized. For the P-mesh simulator it was found that the simplest and most straightforward way to characterize a discontinuity is to find the scattering parameters [1]. The CPW P-mesh algorithm solves for magnetic current distributions and, from this distribution, computes the scattering parameters.

De-embedding arms are the means by which scattering parameters are "measured" once current distributions have been calculated. The de-embedding technique for the CPW is based on the method used in the microstrip version of P-mesh [1]. This basic method and the changes necessary, due to the geometry and the desired mode of operation of the CPW, are summarized here. The current distribution on a few structures is discussed in Section 4.2. The curve-fitting technique is described in Section 4.3. Network excitation and mode extraction are the subjects of Section 4.4 and multi-port network de-embedding and the connection algorithm are discussed in Sections 4.5 and 4.6, respectively.

4.2 Current Distribution

4.2.1 Introduction Before the scattering parameters are calculated for a given network, the magnetic current distribution on the structure

must first be computed. While this current distribution alone is not an adequate means of characterizing a network, it does lend insight into the physical operation of the network and can be a valuable tool in understanding how magnetic current flows in CPWs.

The distribution of a few representative structures will be presented and discussed. All structures have de-embedding arms attached to the ports. In "measuring" the S-parameters, the current on these de-embedding arms is sampled. It is assumed for this de-embedding scheme, that the de-embedding arms have a sinusoidal current distribution, i.e., they are far enough from any discontinuity that higher order modes are negligible. That assumption is verified in this section.

It should be noted that each slot is only one cell wide in the following examples. Due to an error in the viewing program the structures appear to have an extra row of cells in the center. These extra cells should be ignored.

Figure 4.1 shows a short-end CPW stub as it was gridded for P-mesh analysis. The magnitudes of the longitudinal magnetic current and the transverse magnetic current are pictured in Figures 4.2 and 4.3, respectively. From the longitudinal current distribution on the de-embedding arms one can conclude that the sinusoidal standing wave assumption is a valid one. The transverse current is shown to be significant only at transition regions.

The magnetic current distribution on the T-junction (Figure 4.4) also shows a sinusoidal distribution on the de-embedding arms and transverse current at the transition regions only. Because it is an asymmetric structure, the current on the two arms of a port are not necessarily equal as they were in the symmetric case. With port 1 excited the lower arms of ports 2 and 3 have larger

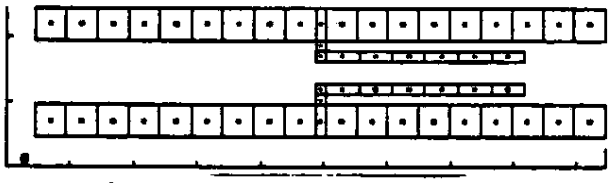

Figure 4.1: Grid of short-end CPW stub.

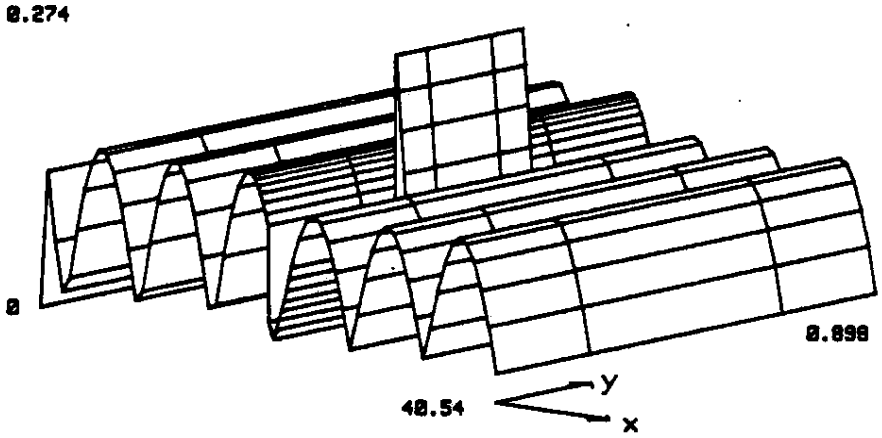

Figure 4.2: Magnitude of longitudinal current on the short-end stub.

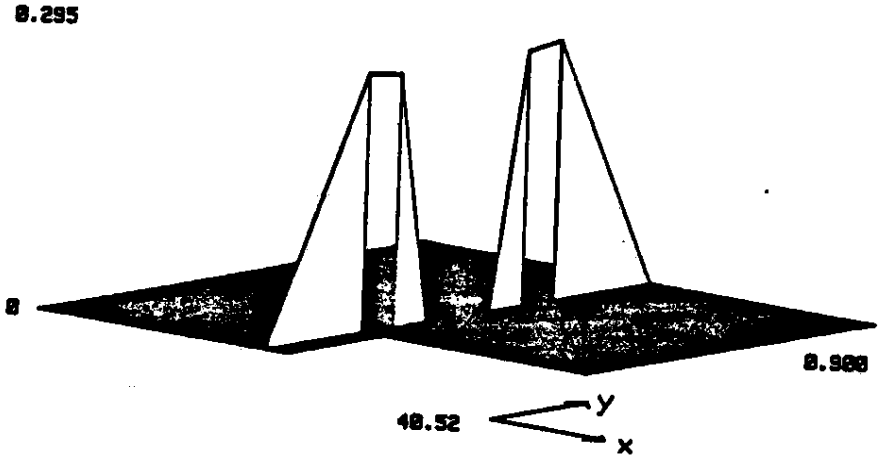

Figure 4.3: Magnitude of transverse current on the short-end stub.

currents than the upper arms (see Figure 4.5). When port 2 is excited the port 1 slot closest to port 2 has a magnetic current distribution that is more than twice as large as that of the other slot (see Figure 4.6). While these results are all rather intuitive it is helpful to compare relative size of the currents for the different slots and understand what happens at points of transition.

4.2.2 Conclusion The major conclusions that can be drawn from the current distribution on these networks are:

- transverse current is significant only in regions of transition
- current distribution on the de-embedding arms approximates a sinusoidal standing wave.

The two structures examined here are analyzed in more detail in Chapter 5.

4.3 Three-Point De-embedding

P-mesh de-embedding implements a three-point curve-fitting technique to extract an "electric current" scattering matrix from microstrip structures. In the case of CPWs, a magnetic current or voltage scattering matrix is extracted instead. This matrix is calculated from the equations derived in Chapters 2 and 3. To apply this technique de-embedding arms are attached to the input and output ports of the structure. A de-embedding arm length of 0.7 wavelengths was found to work well for symmetric structures. For nonsymmetric structures, such as the T-junction, longer arms may be needed. Since the de-embedding arms are assumed to be long enough such that the current distribution on the feedlines is close to sinusoidal, the current standing wave at each port can be sampled, as follows, leading to the incident and reflected

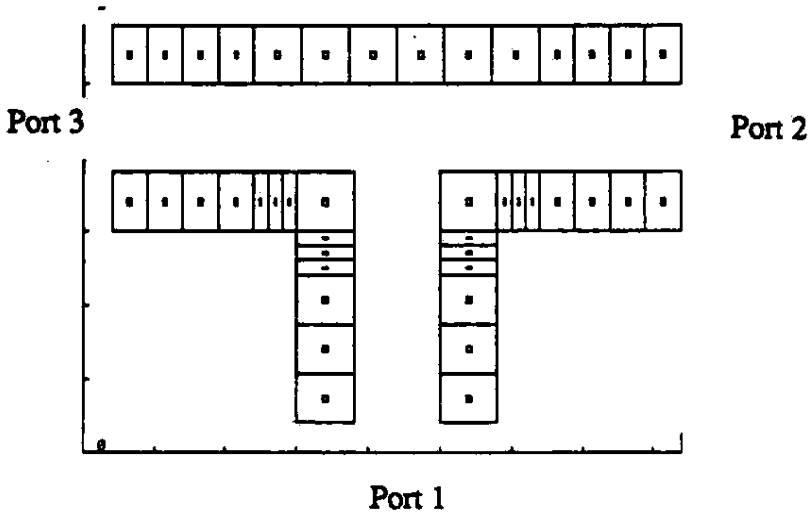

Figure 4.4: Grid of CPW T-junction.

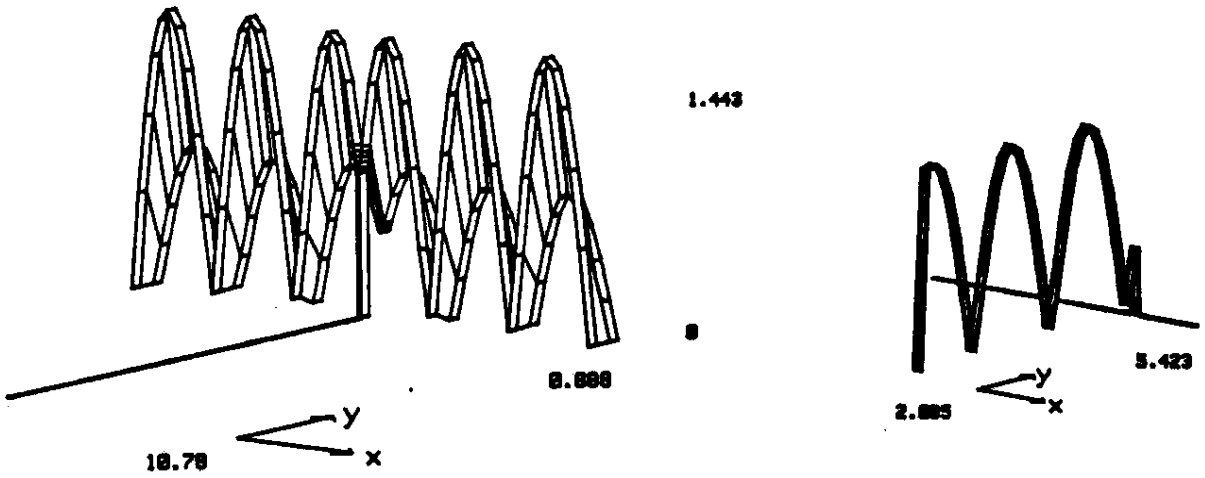

Figure 4.5. Magnitudes of longitudinal and transverse currents when port 1 is excited.

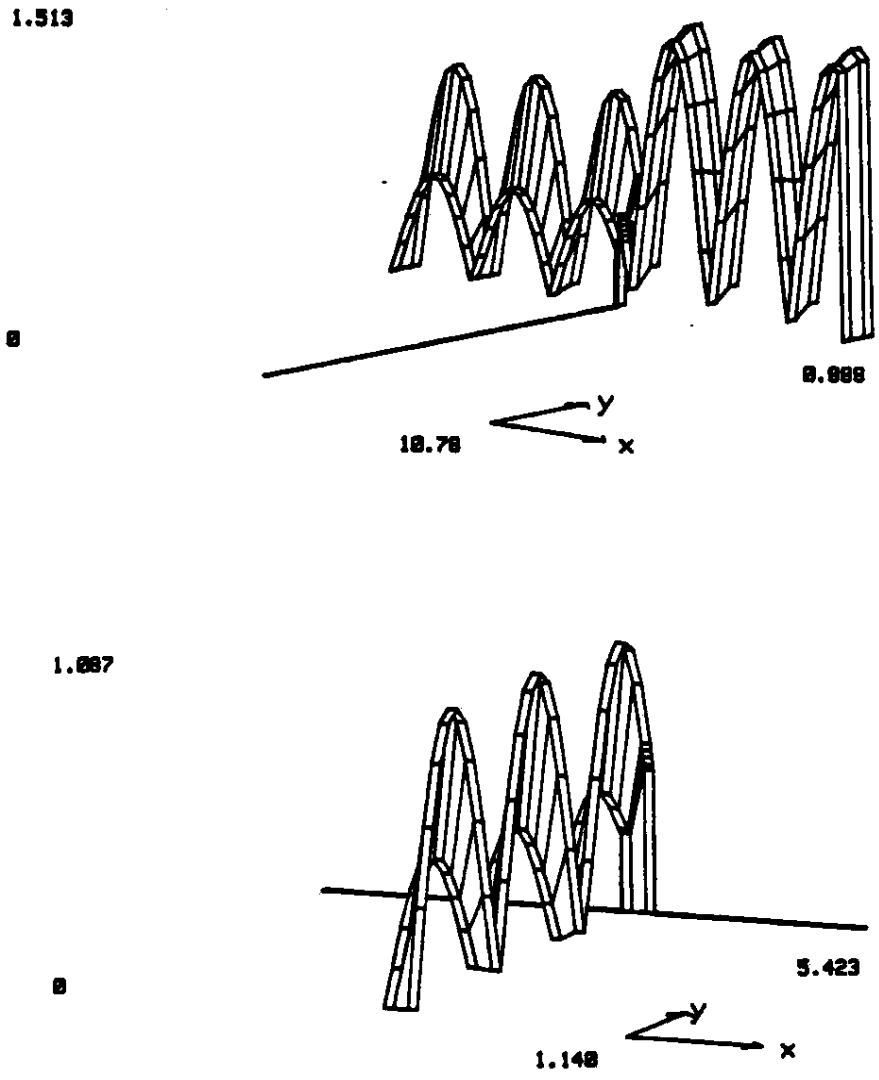

Figure 4.6. Magnitudes of longitudinal and transverse currents when port 2 is excited.

waves and, hence, the scattering parameters.

Assuming a sinusoidal magnetic current distribution, $V(z)$:

$$V(z) = ae^{-\gamma z} + be^{\gamma z} \tag{4.1}$$

where z is the port linear coordinate and $a(= \frac{\tilde{a}}{\sqrt{Z_C}})$ and $b(= \frac{\tilde{b}}{\sqrt{Z_C}})$ are normalized wave variables. Taking three equi-spaced points on the port(see figure 4.7), with the middle point($z = 0$) in the center of the arm, we can write,

$$z = -z_0: \quad V_1 = ae^{\gamma z_0} + be^{-\gamma z_0} \tag{4.2}$$

$$z = 0: \quad V_2 = a + b \tag{4.3}$$

$$z = z_0: \quad V_3 = ae^{-\gamma z_0} + be^{\gamma z_0} \tag{4.4}$$

Combining these three equations yields,

$$\cosh \gamma z_0 = \frac{V_1+V_3}{2V_2} \tag{4.5}$$

$$a = \frac{V_1-V_2e^{-\gamma z_0}}{e^{\gamma z_0}-e^{-\gamma z_0}} \tag{4.6}$$

$$b = -\frac{V_1-V_2e^{\gamma z_0}}{e^{\gamma z_0}-e^{-\gamma z_0}}. \tag{4.7}$$

If $\beta z_0 < \frac{\pi}{2}$ then the solution for γ is unique. With γ known, the incident and reflected waves can be calculated from the equations above and the scattering parameters computed.

4.4 Network Source Excitation and Mode Extraction

From the algorithm developed in the previous chapters the magnetic current distribution on each arm is calculated. However, unlike microstrips, CPWs have two arms per port instead of one. Thus, before the curve-fitting

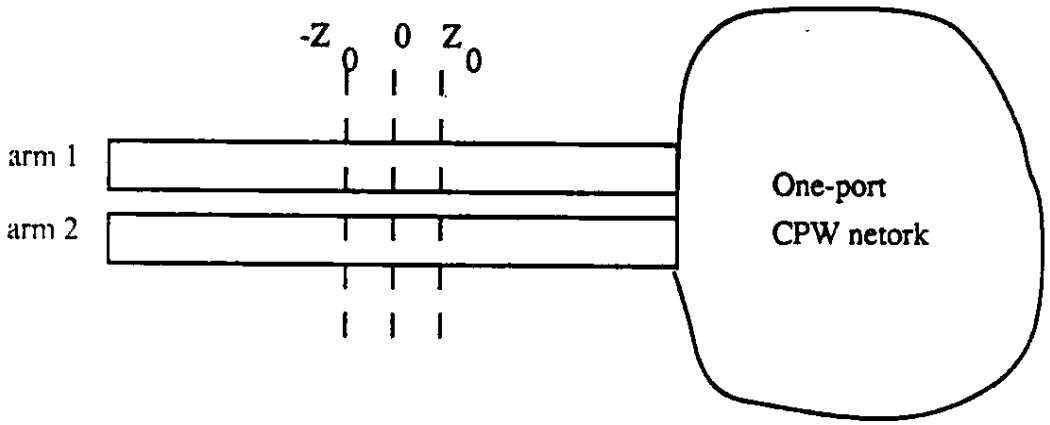

Figure 4.7: One-port coplanar waveguide with de-embedding arms.

technique can be applied the current distribution for each port must be examined more closely. The manner in which this distribution is calculated depends upon the desired mode of operation.

The CPW is capable of supporting either the CPW mode, the coupled slotline mode or a combination of the two. The mode of operation is largely, although not exclusively, determined by the excitation to the network. The CPW mode, or odd mode, is excited by sources, on each arm of a port, of equal magnitude and opposite phase(see figure 4.8). This mode concentrates the fields around the slot aperture and, because it is less dispersive than the coupled slotline mode[3], is commonly used in CPW circuits. At nonsymmetric discontinuities, however, the even(slotline)-mode, as well as an odd-mode, can be generated with an odd mode source excitation. While air-bridges and bonding wires are often used to short out this parasitic mode in MMIC fabrication, incorporating them in the algorithm presented here is beyond the scope of this thesis.

To extract the odd-mode, the mode of interest, the current for each port is defined as the difference between the currents on the arms of the port. In terms of the three-point curve fitting scheme, V_1, V_2 and V_3 become,

$$V_1 = V_1(\text{arm}N) - V_1(\text{arm}N+1) \tag{4.8}$$

$$V_2 = V_2(\text{arm}N) - V_2(\text{arm}N+1) \tag{4.9}$$

$$V_3 = V_3(\text{arm}N) - V_3(\text{arm}N+1) \tag{4.10}$$

and the reflected odd mode wave is calculated as a function of the incident odd mode wave, i.e.,

$$b_1^o = S_{11}^{o,o} a_1^o + S_{12}^{o,o} a_2^o + ... + S_{1N}^{o,o} a_N^o \tag{4.11}$$

$$\begin{bmatrix} +1 & -1 & 0 & 0 & 0 & 0 & 0 & 0 \\ 0 & 0 & -1 & +1 & 0 & 0 & 0 & 0 \\ 0 & 0 & 0 & 0 & +1 & -1 & 0 & 0 \\ 0 & 0 & 0 & 0 & 0 & 0 & -1 & +1 \end{bmatrix}$$

Figure 4.8. Odd mode excitation matrix for a four-port CPW structure. For an N-port network the source excitation would be represented by an $N \times 2N$ matrix.

$$\begin{bmatrix} 1^{90°} & 1^{0°} & 0 & 0 & 0 & 0 & 0 & 0 \\ 1^{0°} & 1^{45°} & 0 & 0 & 0 & 0 & 0 & 0 \\ 0 & 0 & 1^{90°} & 1^{0°} & 0 & 0 & 0 & 0 \\ 0 & 0 & 1^{0°} & 1^{45°} & 0 & 0 & 0 & 0 \\ 0 & 0 & 0 & 0 & 1^{90°} & 1^{0°} & 0 & 0 \\ 0 & 0 & 0 & 0 & 1^{0°} & 1^{45°} & 0 & 0 \\ 0 & 0 & 0 & 0 & 0 & 0 & 1^{90°} & 1^{0°} \\ 0 & 0 & 0 & 0 & 0 & 0 & 1^{0°} & 1^{45°} \end{bmatrix}$$

Figure 4.9. Combined odd/even mode excitation matrix for a four-port CPW structure.

While extracting the odd mode in this manner is sufficient for symmetric networks, problems arise in nonsymmetric junctions where an even mode that is no longer negligible is generated. Power converted from odd to even and then back to the odd mode is not being accounted for. When the even mode resonates this can cause problems. To rectify this it is necessary to take into account the even mode as an odd mode source. Doing this the reflected wave becomes,

$$b_1^o = S_{11}^{o,o} a_1^o + S_{11}^{o,e} a_1^e + ... + S_{1N}^{o,o} a_N^o + S_{1N}^{o,e} a_N^e. \tag{4.12}$$

In matrix form we have,

$$\begin{pmatrix} b_1^o \\ b_1^e \\ b_2^o \\ b_2^e \\ \vdots \\ b_N^o \\ b_N^e \end{pmatrix} = \begin{bmatrix} S_{1,1}^{o,o} & S_{1,1}^{o,e} & S_{1,2}^{o,o} & \cdots & S_{1,N}^{o,e} \\ S_{1,1}^{e,e} & S_{1,1}^{o,e} & S_{1,2}^{e,e} & \cdots & S_{1,N}^{o,e} \\ S_{2,1}^{o,o} & S_{2,1}^{o,e} & S_{2,2}^{o,o} & \cdots & S_{2,N}^{o,e} \\ S_{2,1}^{e,e} & S_{2,1}^{o,e} & S_{2,2}^{e,e} & \cdots & S_{2,N}^{o,e} \\ \vdots & \vdots & \vdots & \ddots & \vdots \\ S_{N,1}^{o,o} & S_{N,1}^{o,e} & S_{N,2}^{o,o} & \cdots & S_{N,N}^{o,e} \\ S_{N,1}^{e,e} & S_{N,1}^{o,e} & S_{N,2}^{e,e} & \cdots & S_{N,N}^{o,e} \end{bmatrix} \begin{pmatrix} a_1^o \\ a_1^e \\ a_2^o \\ a_2^e \\ \vdots \\ a_N^o \\ a_N^e \end{pmatrix} \tag{4.13}$$

To satisfy this equation the even mode must also be extracted from the magnetic current distribution. To do this the odd mode network excitation is replaced with one that will purposely generate even and odd-modes(see figure 4.9), to prevent errors from very small even-modes. This network excitation was chosen randomly and found to work well. The even mode is extracted by adding the current along the arms of the port. With this method each port has an odd mode and an even mode incident and reflected wave. As a result, the calculation of the odd mode is more accurate and the value of the even mode generated is now known.

4.5 Multi-Port Network De-embedding

From section 4.2 the S-parameters for a one-port network can easily be solved. To find the scattering parameters for a multiple-port network a, b and γ for each port and each excitation must be detected. If all ports have the same transverse geometry then Equation, 4.13, only is needed and we are left with N^2 equations and N^2 unknowns.

For ports of different transverse geometries, i.e. different characteristic impedances, we have to let

$$S'_{i,j} = \sqrt{S_{i,j}S_{j,i}} \tag{4.14}$$

and assume $S'_{i,j} = S'_{j,i}$, for passive, isotropic networks, to account for wave normalization and to avoid the need to define the characteristic impedances.

4.6 A General Network Connection Algorithm

The general network connection algorithm is the same as that used in the microstrip version of P-mesh.[1] In short, the new S-matrix, S', for connected networks A and B(see figure 4.10) is,

$$[S'] = ([I] - [S^A][S^B]_g)^{-1}[S^A][T] \tag{4.15}$$

where $[S^B]_g$ is the global S-matrix for network B, the smaller of the two, and $[T]$ is the identity matrix $[I]$ with the 1's in the (i,i)-th and (j,j)-th elements replaced with 0's. The reader is referred to [1] for further details.

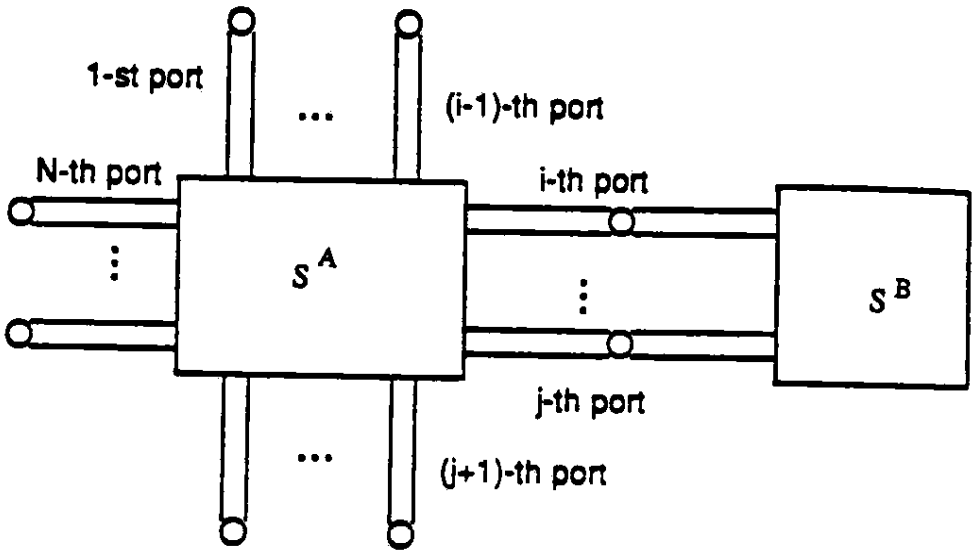

Figure 4.10: A network connection.

CHAPTER 5

CPW CIRCUITS

5.1 Introduction

The P-mesh algorithm for coplanar waveguides is useful only if it is accurate. To prove its accuracy, this algorithm was applied to symmetric and nonsymmetric junctions consisting of a section of transmission line, open and short-end CPW stubs, a T-junction and a two-stub CPW-slotline transition. The theoretical results for the waveguide wavelength, the effective dielectric constant and the scattering parameters are compared to measured and theoretical results from other sources.

A cross-section of the CPW model is shown in Figure 5.1. The reader is referred to Section 1.2 for a discussion of some of the techniques presented in this chapter.

5.2 CPW Transmission Line Parameters

A section of CPW transmission-line (h = 0.635 mm, ϵ_{r2} = 10.03) was analyzed with P-mesh for two geometries. The theoretically derived data demonstrated a frequency dependence for the waveguide wavelength ratio, $\frac{\lambda_g}{\lambda_0}$, which is to be expected since $\frac{\lambda_g}{\lambda_0}$ is inversely proportional to $\sqrt{\epsilon_{reff_g}}$, which, in turn, increases with frequency. This agrees closely with data calculated from Cohn's equations and measured results [26] (See Figure 5.2). The quasi-static results from Wen are also given.

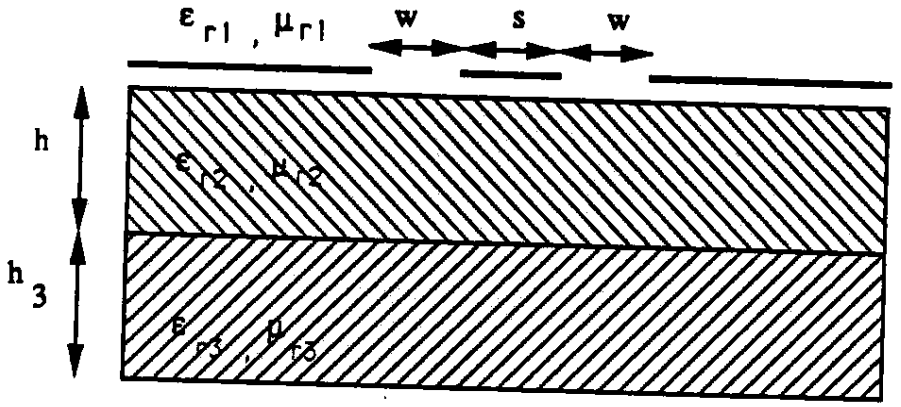

Figure 5.1: Coplanar Waveguide.
Assume $\epsilon_{r1} = \epsilon_{r3} = \mu_{r1} = \mu_{r2} = \mu_{r3} = 1$ and $h_3 = \infty$, unless stated otherwise.)

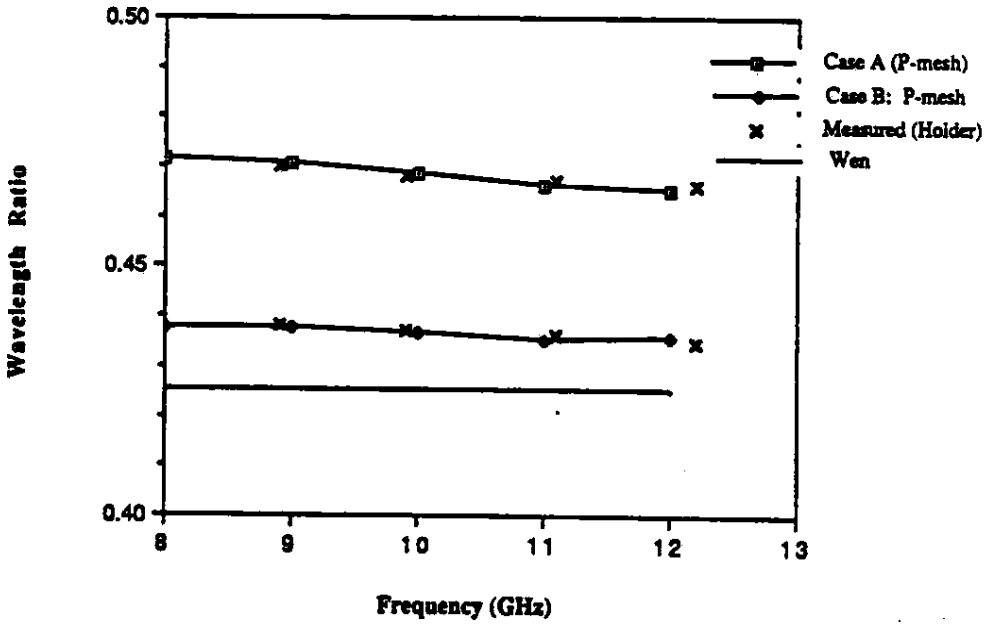

Figure 5.2: CPW waveguide wavelength as a function of frequency.
Case A: w= 0.05 mm, s= 1.17 mm.
Case B: w= 0.21 mm, s= 0.5 mm.

Since the effective dielectric constant,

$$\epsilon_{reff} = \frac{c^2}{\lambda_g^2 f^2}, \tag{5.1}$$

is simply dependent on λ_g it is comparably accurate.

5.3 CPW Short-End and Open-End Stubs

The short-end and open-end series stubs, shown in Figures 5.3 and 5.4, serve as filter elements. When the stub in the center of Figure 5.3 has a length of $\frac{\lambda_g}{4}$ it will short out Port 1, resulting in total reflection. For the stub in Figure 5.4, a stub length of $\frac{\lambda_g}{4}$ will produce an open circuit resulting in total transmission from Port 1 to Port 2. A theoretical and experimental analysis of these stubs has been carried out by Dib, Katehi, Ponchak and Simons [18]. The scattering parameters for the short-end and open-end CPW stubs, derived from P-mesh compare favorably with both the measured and theoretical values from [18]. The magnitudes and phases for pertinent S-parameters are given in Figures 5.5 -5.8. For the short-end stub, resonant frequency as a function of stub length was also measured. Since a stub of length $\frac{\lambda_g}{4}$ will resonate, the relationship between resonant frequency and stub length can be expressed as

$$f_{res} = \frac{c}{4L\sqrt{\epsilon_{reff}}}. \tag{5.2}$$

Since f_{res} is dependent on ϵ_{reff}, as well as L, the relationship between f_{res} and L will not be linear. The results shown in Figure 5.10 agree well with each other and with Equation 5.2.

Small discrepancies between theoretical results and measured results may be due to differences in the models used. The theoretical model in [18] was assumed to be in a cavity. Radiation, conductor and dielectric losses

weren't included in this analysis. Experimental data was taken from open, lossy structures. The P-mesh model is also for an open structure, and it does include radiation loss, though not conductor or dielectric losses.

5.4 T-Junction

While microstrip T-junctions have been studied extensively, not much information is available for CPW T-junctions. To further complicate matters, T-junctions without air-bridges are difficult to measure. Measurement probes often short circuit the ground planes [14]. Utilizing a three-dimensional finite-difference technique, Shibata and Sano [14] analyzed the CPW T-junction, shown in Figure 5.11, with and without air-bridges. The scattering parameters for the latter structure were derived with P-mesh. Comparison of the results (Figure 5.12) show that, with the ground planes unconnected, the structure does not act like a T-junction. While the reflection, $|S_{11}|$, decreases with the removal of the air-bridges, the transmitted signal, $|S_{21}|$, also decreases, indicating a large, undesired, conversion to the even mode.

5.5 Two-Stub CPW-Slotline Transition

A method to excite propagation along slotlines, proposed by Houdart, and examined in more detail by Hanna and Ramboz [8], is the two-stub CPW-slotline transition. Being a planar transition, it is reproductable and easy to fabricate, thus, giving it an edge over coaxial-slotline transitions and microstrip-slotline transitions.

Using an equivalent circuit approach and optimizing slotline and stub lengths, Hanna and Ramboz designed and analyzed the CPW-slotline transition given in Figure 5.13. Analysis of the same structure, without bonding

wires, by P-mesh gives very different results (see Figure 5.14). As in the T-junction case, this complex structure, with its grounds unconnected, demonstrates a large even mode propagation.

5.6 Conclusion

From the examples in the previous sections the CPW P-mesh algorithm appears to be an effective modeling tool for MMIC design. The data presented demonstrate good agreement between P-mesh, actual measurements and other theories. Dielectric and conductor loss, which are not included in the CPW P-mesh algorithm, do not appear to have a significant effect in these examples. However, the inability to model air-bridges and bonding wires rules out the use of the P-mesh simulator in the analysis of more complex structures, such as T-junctions and the CPW-slotline transition, which need air-bridges or bonding wires to operate in the desired manner.

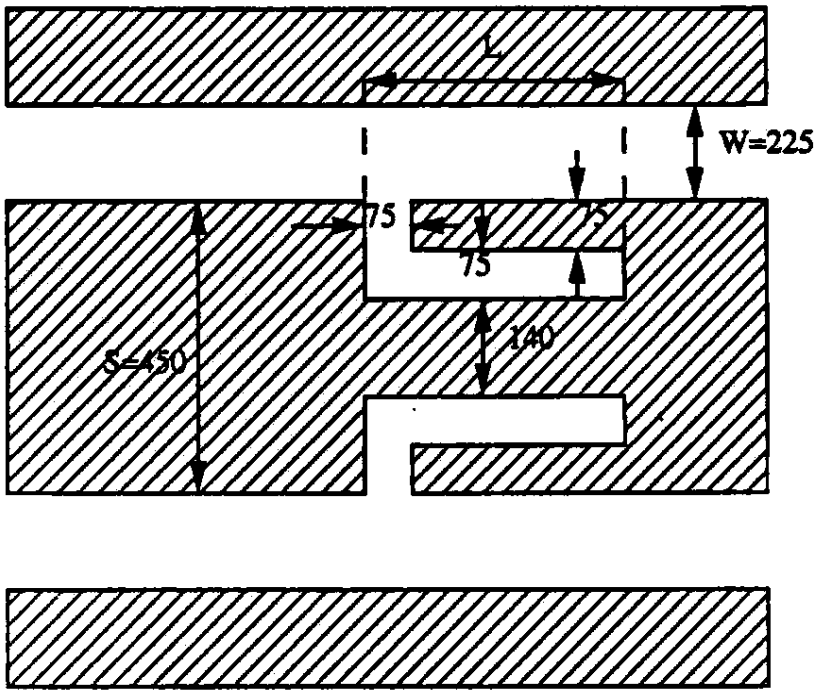

Figure 5.3: Short-end CPW stub with L=1500 μm.
(h = 25mil, h_3 = 125mil, $\epsilon_{r2} = 9.9, \epsilon_{r3} = 2.2$; other dimensions in μm.)

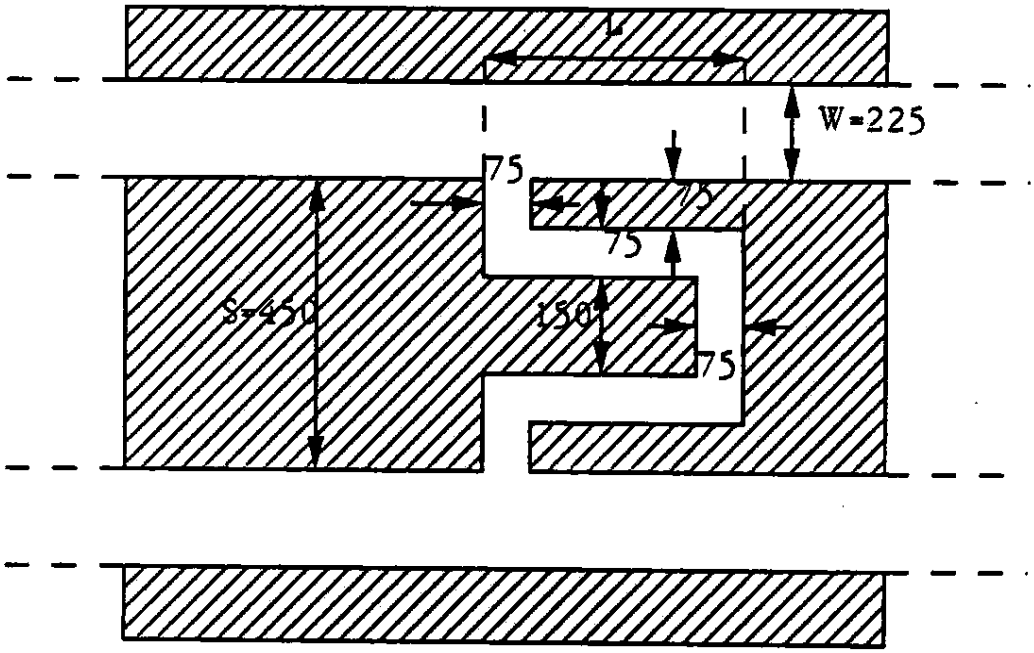

Figure 5.4: Open-end CPW stub with L=1500 μm.
(h = 25mil, h_3 = 125mil, $\epsilon_{r2} = 9.9, \epsilon_{r3} = 2.2$; other dimensions in μm.)

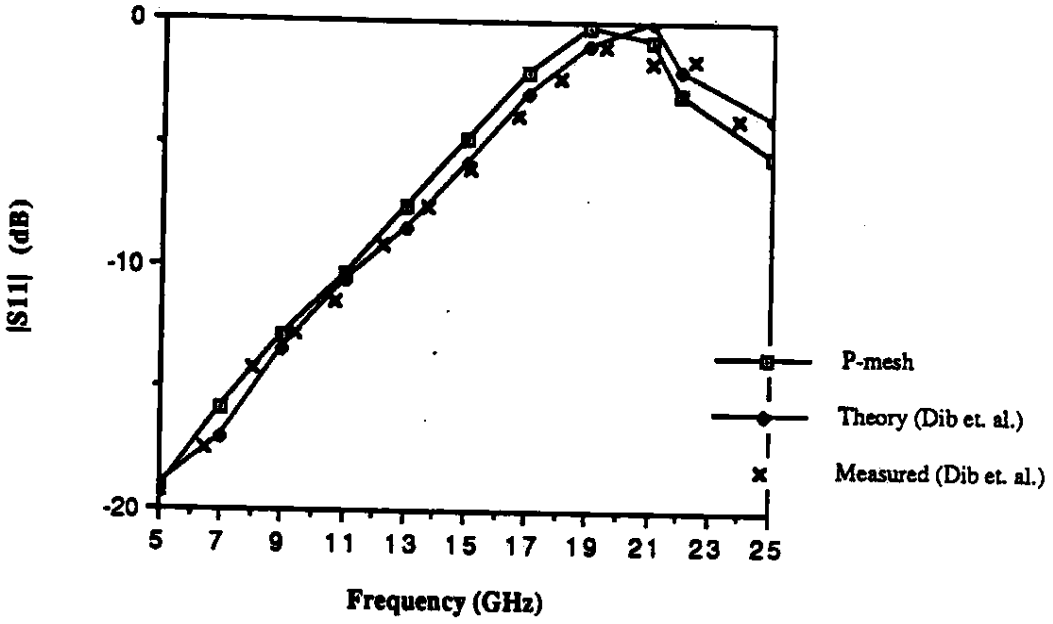

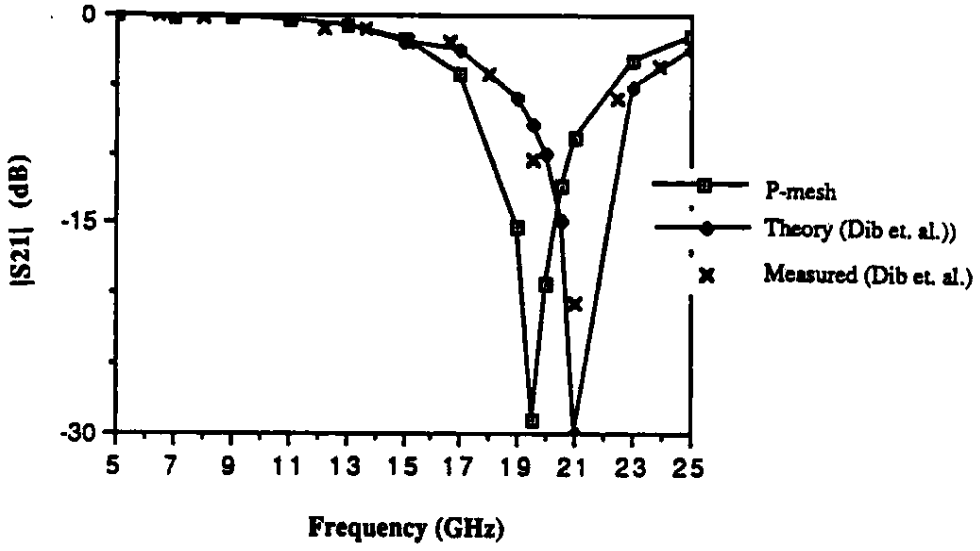

Figure 5.5: $|S_{11}|$ and $|S_{21}|$ for short-end CPW stub.

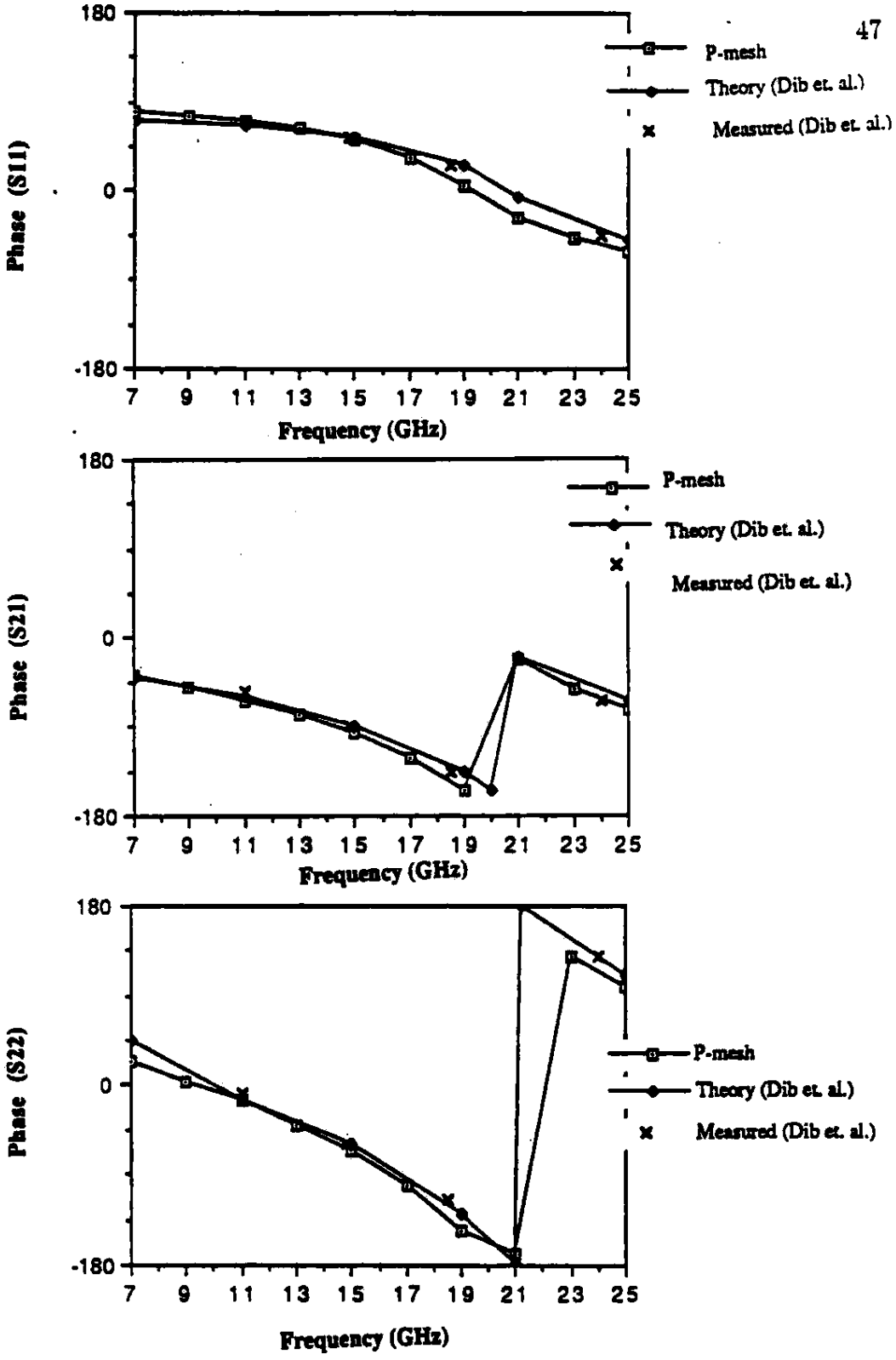

Figure 5.6: Phase response of short-end CPW stub.

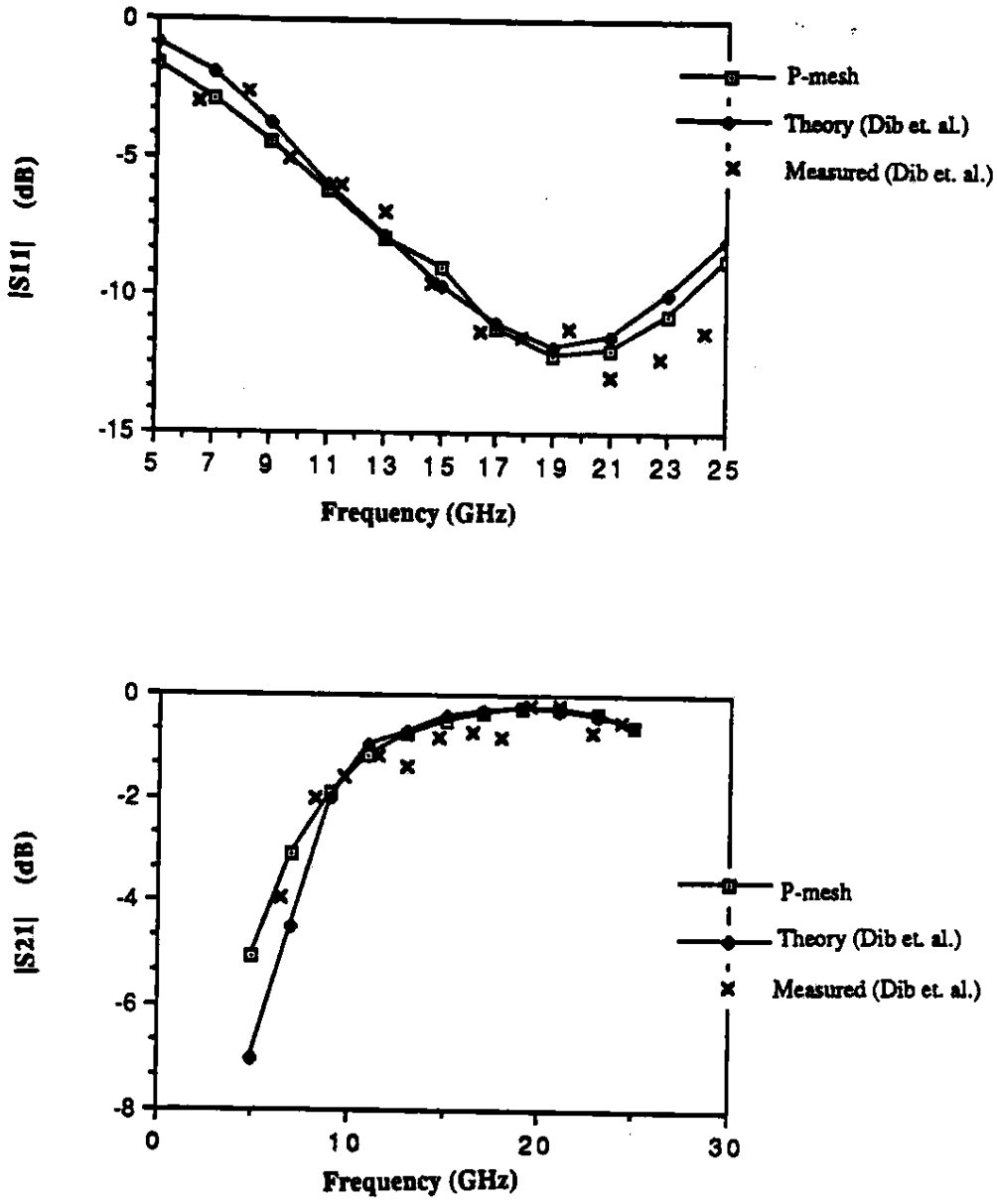

Figure 5.7: $|S_{11}|$ and $|S_{21}|$ for open-end CPW stub.

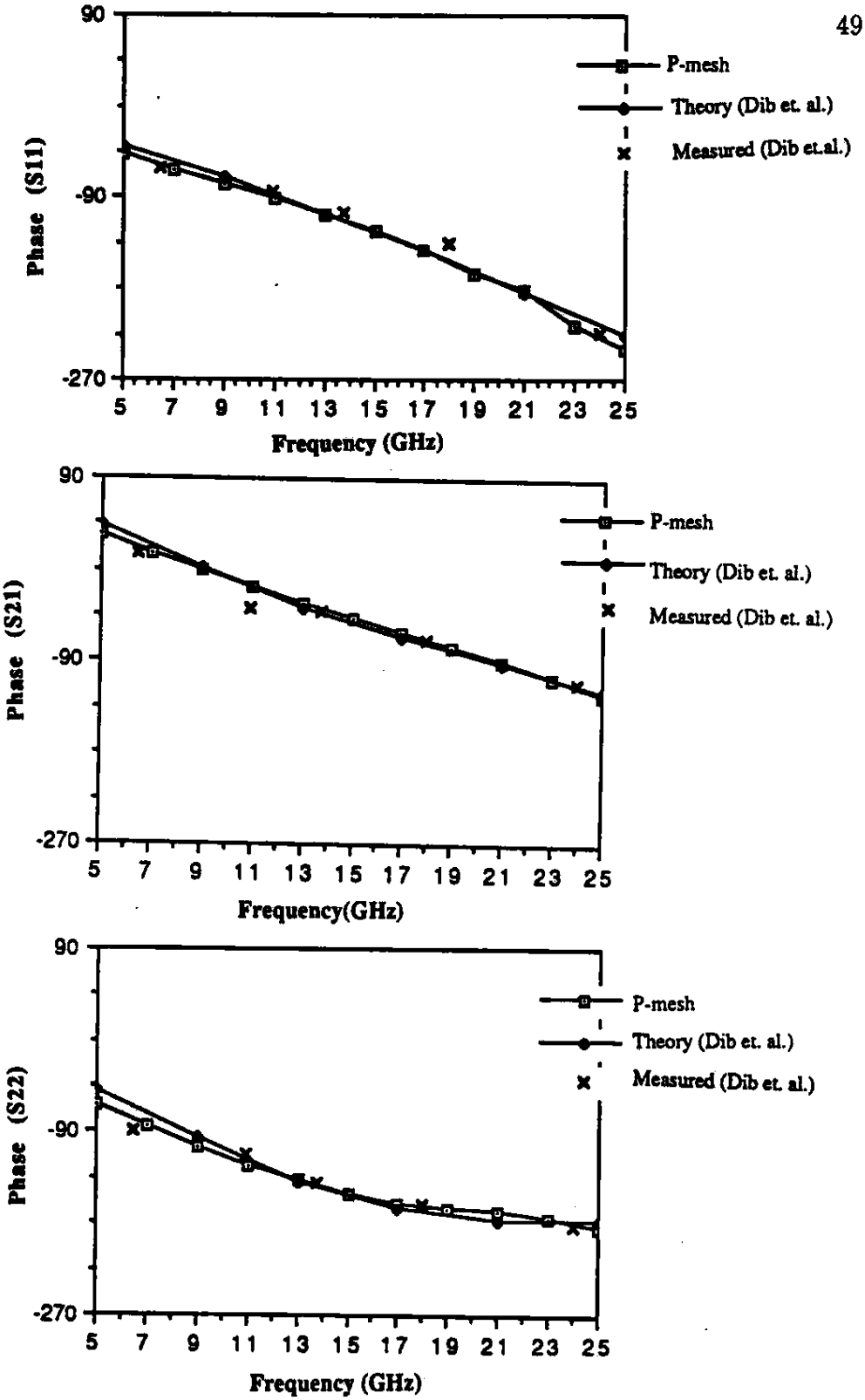

Figure 5.8: Phase response of open-end CPW stub.

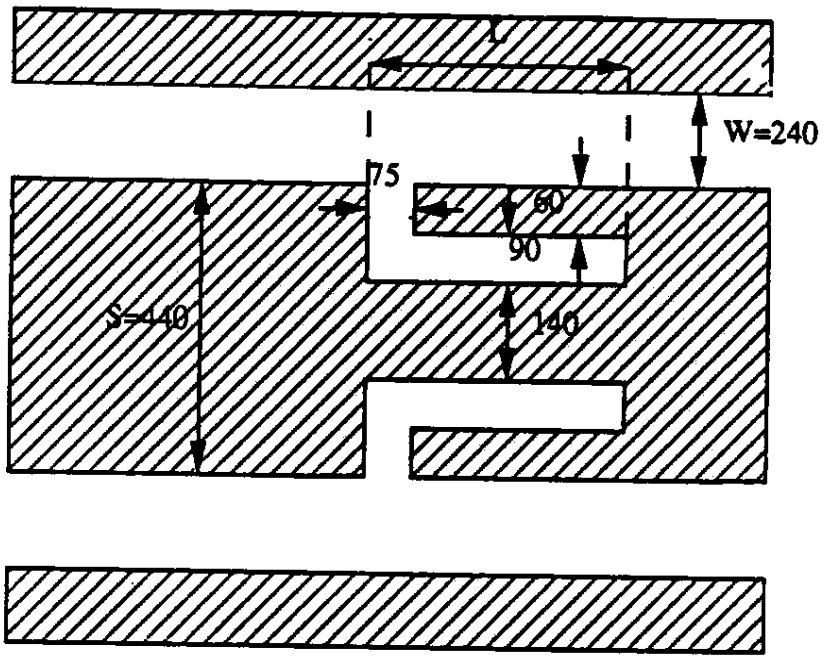

Figure 5.9: Short-end CPW stub with variable stub length, L.
($h = 25\text{mil}, h_3 = 125\text{mil}, \epsilon_{r2} = 9.9, \epsilon_{r3} = 2.2$; other dimensions in μm)

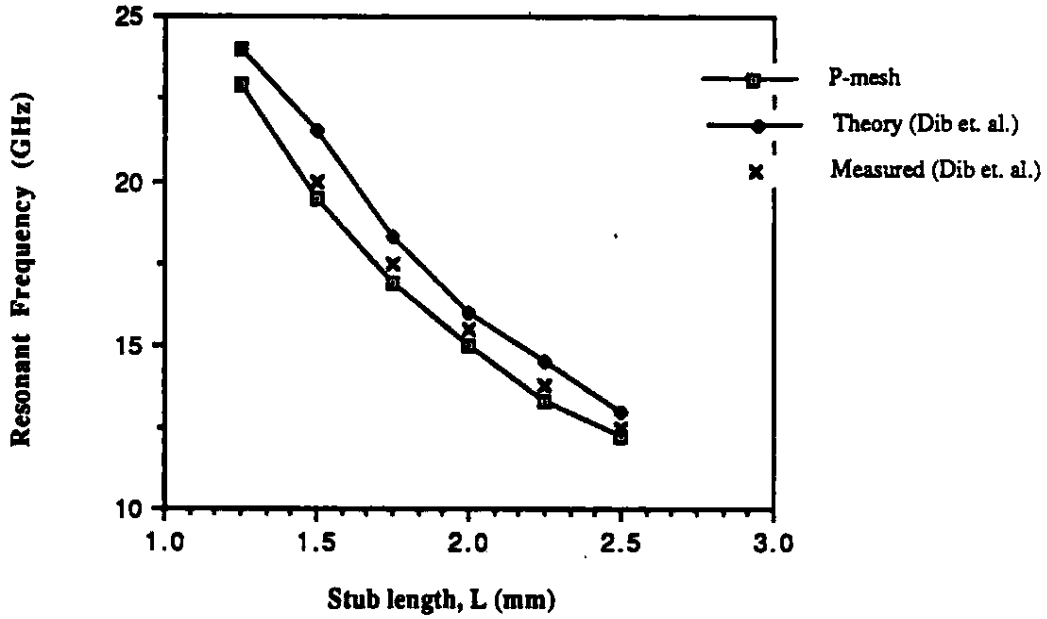

Figure 5.10: Resonant frequency as a function of stub length.

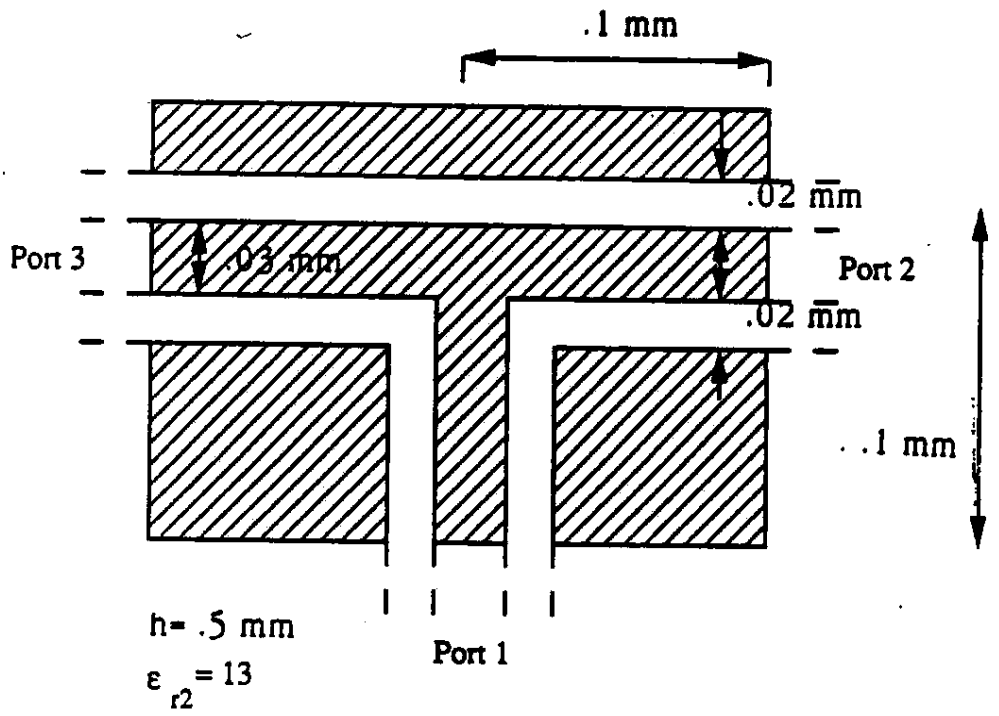

Figure 5.11: T-junction

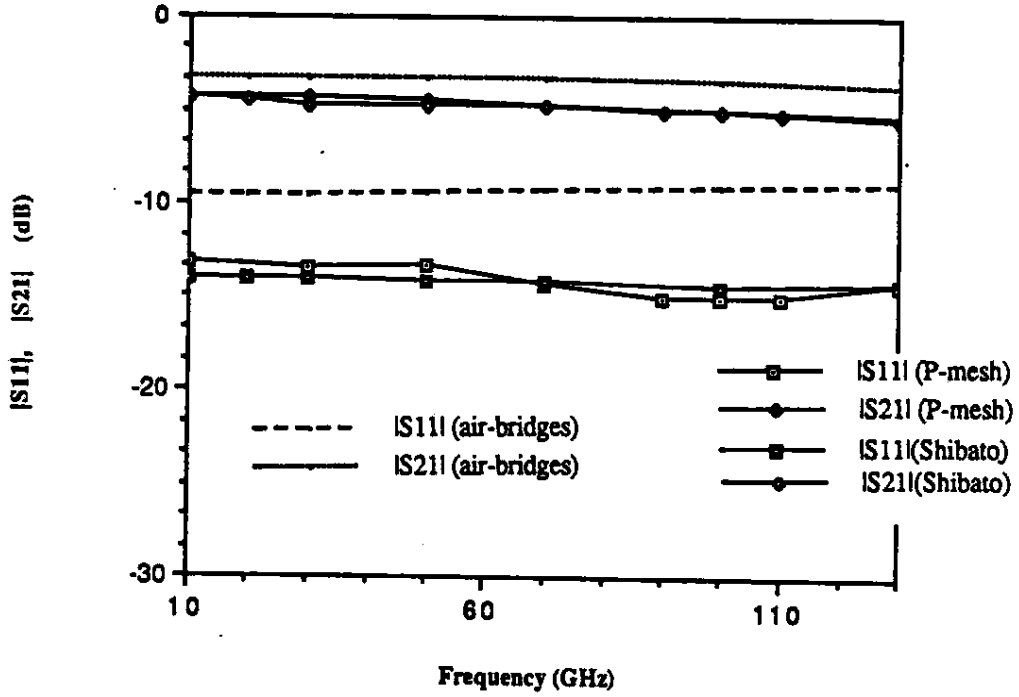

Figure 5.12: $|S_{11}|$ and $|S_{21}|$ for CPW T-junction.

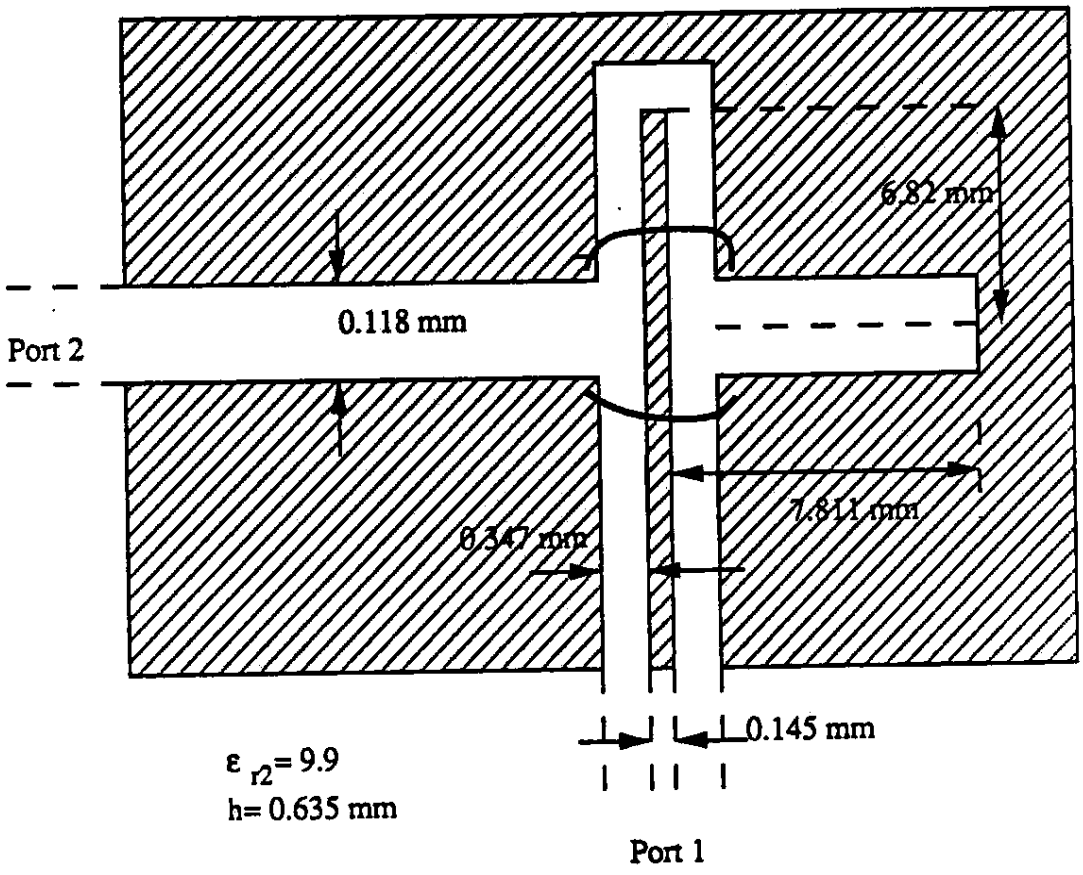

Figure 5.13: Two-stub CPW-slotline transition.

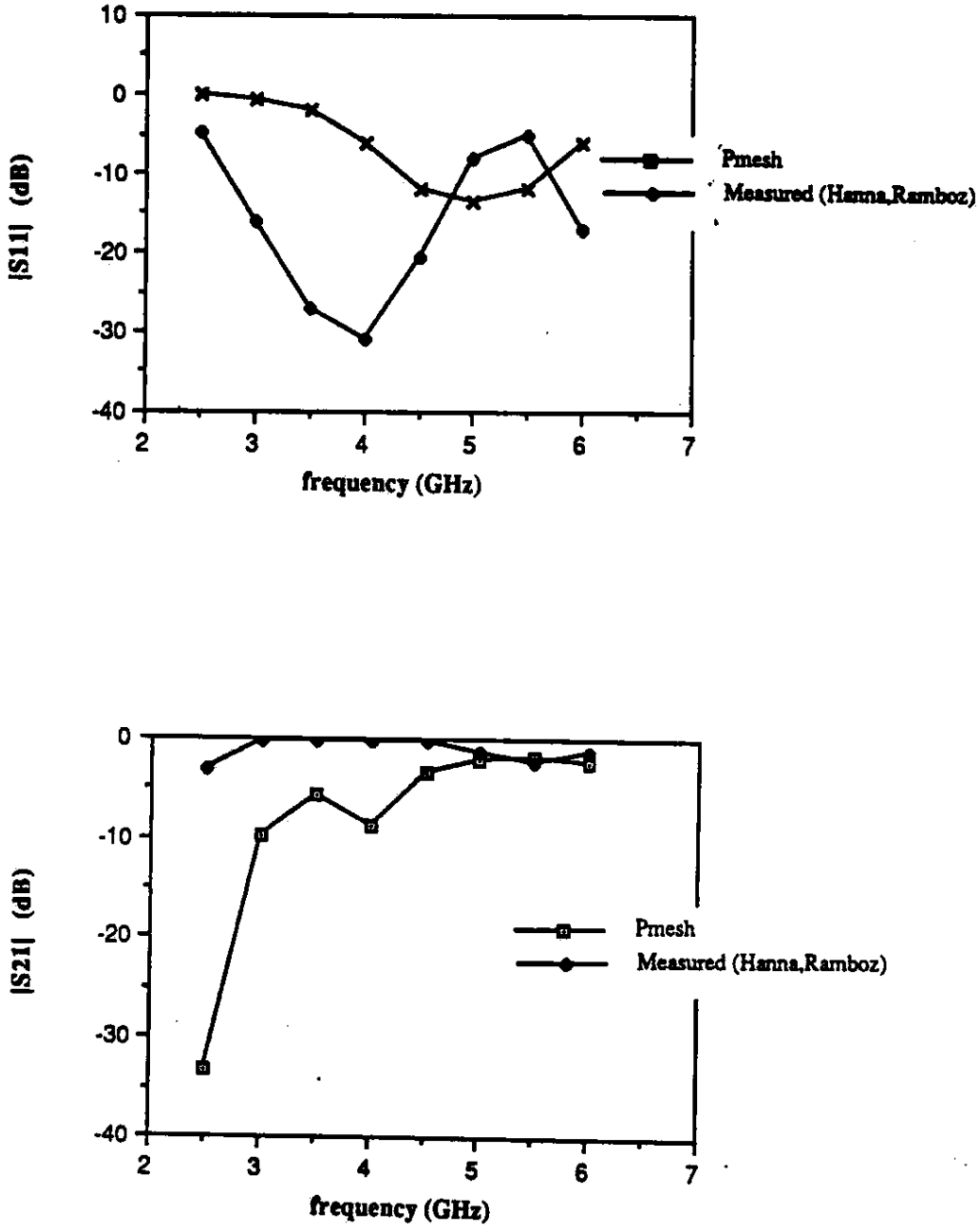

Figure 5.14: $|S11|$ and $|S21|$ for CPW-slotline transition.

CHAPTER 6

CONCLUSION

The goal of this thesis was to adapt the P-mesh theory to coplanar waveguides and implement it in a CAD program.

The first step in achieving this goal was the derivation of the MPIE for the CPW. Assuming an impressed magnetic current in the slots and applying the boundary conditions, the MPIE and the Green's functions were derived. The magnetic and electric Green's functions were simplified to one-dimensional Sommerfeld integrals which can be calculated by numerical integration.

The MPIE was solved for the magnetic current with the moment method. One of the distinctive features of P-mesh is the choice of roof-top basis functions for rectangular and triangular cells as the basis and testing functions. With rectangular cells modeling regular regions and triangular cells modeling irregular regions, the algorithm gains flexibility and improved accuracy.

With the current distribution for the structure known, P-mesh becomes a valuable tool in understanding what happens physically to current at CPW discontinuities.

To characterize a network, the current distribution is sampled and the scattering parameters calculated. With an odd/even mode excitation the odd and even mode currents for each port are calculated. The three-point curve-fitting technique in conjunction with a network connection algorithm leads to the derivation of the scattering parameters.

For various CPW structures the P-mesh derived data was found to be in accordance with measured and theoretical data from other sources.

For use in MMIC design the algorithm was implemented in a CAD program. A program to calculate the CPW Green's functions, by Ahmad Hoorfar, was integrated into the P-mesh program, developed by Jian X. Zheng. Major changes to this code included the source excitation and de-embedding sections.

For the structures analyzed, the CPW P-mesh code performed well. However, for more complex structures floating grounds are unrealistic. The incorporation of air-bridges and bonding wires into the program will greatly extend the number of practical MMIC structures which can be analyzed with the CPW P-mesh. The addition of dielectric and conductor loss is also desirable.

BIBLIOGRAPHY

[1] J. X. Zheng, "Modeling of microstrip discontinuities and antennas of arbitrary shape,"Ph. D. thesis, University of Colorado at Boulder, 1990.

[2] R. W. Jackson, "Mode conversion at discontinuity in finite-width conductor-backed coplanar waveguides," **IEEE Trans. on Microwave Theory and Tech.**, Vol. MTT-37, pp. 1582-1589, Oct. 1989.

[3] R. W. Jackson, "Considerations in the use of coplanar waveguide for millimeter-wave integerated circuits," **IEEE Trans. on Microwave Theory and Tech.**, Vol. MTT-34, pp. 1450-1456, Dec. 1986.

[4] C. N. Chang, Y. C. Wong and C. H. Chen, "Full-wave analysis of coplanar waveguides by Variational conformal mapping technique," **IEEE Trans. on Microwave Theory and Tech.**, Vol. MTT-38, pp. 1339-1343, Sept. 1990.

[5] C. P. Wen, "Coplanar-waveguide directional couplers," **IEEE Trans. on Microwave Theory and Tech.**, Vol. MTT-18, pp. 318-322, June 1970.

[6] R. E. Stegens, "Coplanar waveguide FET amplifiers for satellite communications systems," **Comsat Technical Review**, Vol. 9, No. 1, pp. 255-267, Spring 1979.

[7] R. N. Simons and G. E. Ponchak, "Modeling of some coplanar waveguide discontinuities," **IEEE Trans. on Microwave Theory and Tech.**, Vol. MTT-36, pp. 1796-1803, Dec. 1988.

[8] V. F. Hanna and L. Ramboz, "Broadband planar coplanar waveguide-slotline transition ," **12th European Microwave Conference, Helsinki, Finland**, pp628-631, 13-17 September 1982.

[9] M. Drissi, F. Hanna and J. Citerne, "Analysis of coplanar waveguide radiating end effects using the integral equation technique," **IEEE Trans. on Microwave Theory and Tech.**, Vol. MTT-39, pp. 112-116, Jan. 1991.

[10] M. Riaziat, E. Par, G. Zdasiuk, S. Bandy and M. Glenn, "Monolithic millimeter wave CPW circuits," **IEEE Trans. on Microwave Theory**

and Tech. Symposium Dig., pp. 525-527, 1989.

[11] C. P. Wen, "Coplanar waveguide: a surface strip transmission line suitable for nonreciprocal gyromagnetic device applications," **IEEE Trans. on Microwave Theory and Tech.**, Vol. MTT-17, pp. 1087-1090, Dec. 1969.

[12] M. E. Davis, E. W. Williams and A. C. Celestini, "Finite-boundary corrections to the coplanar waveguide analysis," **IEEE Trans. on Microwave Theory and Tech.**, Vol. MTT-21, pp. 594-596, Sept. 1973.

[13] K. C. Gupta, R. Garg, I. J. Bahl, **Microstrip Lines and Slotlines**, Artech House, Inc.; Dedham, MA, 1979.

[14] T. Shibata and E. Sano, "Analysis of coplanar lines utilizing the finite difference time-domain technique," **Electronics and Communications in Japan, Part 2**, Vol. 73, No. 11, pp. 38-49, 1990.

[15] M. Naghed and I. Wolff, "A three-dimensional finite-difference calculation of equivalent capacitances of coplanar waveguide discontinuities," **IEEE Trans. on Microwave Theory and Tech. Symposium Dig.**, pp. 1143-1146, 1990.

[16] R. F. Harrington, **Field Computations by Moment Methods**, Macmillan; New York, 1968.

[17] J. B. Knorr and K. D. Kuchler, "Analysis of coupled slots and coplanar strips on dielectric substrate," **IEEE Trans. on Microwave Theory and Tech.**, Vol. MTT-23, pp. 541-547, July 1975.

[18] N. I. Dib, L .P. B. Katehi, G. E. Ponchak and R. N. Simons, "Theoretical and experimental characterization of coplanar waveguide discontinuities for filter applications," **IEEE Trans. on Microwave Theory and Tech.**, Vol. MTT-39, pp. 873-882, May 1991.

[19] D. C. Chang and J. X. Zheng, "Electromagnetic modeling of passive circuit elements in MMIC," to be published.

[20] D. I. Wu, D. C. Chang, and B. L. Brim, "Accurate numerical modeling of microstrip junctions and discontinuities," **Int. Journal of Microwave and Millimeter-wave Computer Aided Design**, Vol. 1, No. 1, pp. 48-58, 1991.

[21] D. C. Chang, D. I. Wu, J. X. Zheng, "Numerical modeling of passive networks and components in monolithic microwave integrated circuits

(MMICs)," to be published.

[22] J. R. Mosig, "Arbitrarily shaped microstrip structures and their analysis ith a mixed potential integral equation," **IEEE Trans. on Microwave Theory and Tech.**, Vol. MTT-36, pp. 314-323, Feb. 1988.

[23] E. F. Kuester and D. C. Chang, **Electromagnetic Boundary Problems**, course notes for ECEN5144, University of Colorado, 1990.

[24] H. Maramis, notes 1990.

[25] A. Hoorfar, E. F. Kuester and D. C. Chang, "Development of efficient codes for computing Green's functions of structures with a multi-layered substrate," MIMICAD presentation, University of Colorado at Boulder, Oct. 1990.

[26] P. A. R. Holder,"X-band microwave ingrated circuits using slotline and coplanar waveguide," **The Radio and Electronic Engineer**, Vol. 48, No. 1/2, pp. 38-42, Jan./Feb. 1978.